Generation of active oxygen species by CO_2 dissociation over defect-rich Ni-Pt/CeO_2 catalyst for boosting methane activation in low-temperature dry reforming: Experimental and theoretical study

Rubina Khatun [a,b], Rohan Singh Pal [a,b], Mohammad Ahmad Shoeb [a], Deepak Khurana [a,b], Shubham Singhl [a], Nazia Siddiqui [a], Mukesh Kumar Poddar [a], Tuhin Suvra Khan [a,b], Rajaram Bal [a,b,*]

[a] *Light Stock Processing Division, CSIR-Indian Institute of Petroleum, Dehradun 248005, India*
[b] *Academy of Scientific and Innovative Research, Ghaziabad, Uttar Pradesh 201002, India*
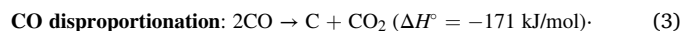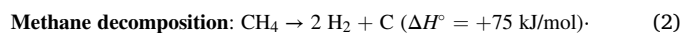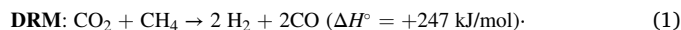
ARTICLE INFO

ABSTRACT

Herein, we demonstrated a one-pot complex combustion method to synthesize defect-rich Ni-Pt/CeO_2 catalyst having oxygen vacancy sites (V_o) by incorporating Ni and Pt species into the ceria lattice. These V_o sites are highly active for dissociating CO_2 into reactive oxygen species and CO at low temperature. CH_4-TPSR demonstrated that surface reactive oxygen species are more selective than lattice oxygen toward the formation of syngas. The catalytic properties and activity of the synthesized catalysts were also compared with the conventionally impregnated catalyst. *In-situ* DRIFT and Raman study revealed reactive oxygen-assisted CH_4 activation via the formation of CH_xO intermediate. DFT calculation also showed the facile formation of CH_3O and CH_2O species over the bimetallic NiPt-CeO_2(111) catalyst surface. The Ni-Pt/CeO_2 (0.5 wt%Pt-2 wt%Ni) catalyst showed superior activity and stability with ~86% conversion of CH_4 and CO_2 at 675 °C, where the H_2/CO ratio is one. The catalyst was stable up to 700 h time-on-stream.

1. Introduction

Global warming is a major concern of our industrialized society, and its adverse effect on the environment is getting more severe with time. To limit CO_2 emissions, the Paris agreement in December 2015 was accepted by 196 countries to reduce greenhouse gas emissions for climate change [1]. This agreement was devoted to keeping global warming below 2 °C and to "continue efforts" to keep it below 1.5 °C by 2100 [1,2]. Therefore, mitigation and utilization of greenhouse gases as valuable feedstocks have become the most compelling area in green energy research. In this aspect, one viable option is the catalytic dry reforming of methane, which mitigates two of the most potent greenhouse gases by converting them into syngas (a mixture of CO and H_2), which has gained massive attention in recent decades [3]. Syngas is one of the versatile intermediate and building blocks for producing high-value-added chemicals and synthetic fuels [4]. Despite its environmental and economic benefits, DRM has not been regarded as fully mature on the industrial level because of the severe catalyst deactivation

by coke deposition and sintering [5,6]. The DRM is highly endothermic in nature (Eq. 1) and requires high operating temperature (600–1000 °C), which leads to the sintering of active metals and coke deposition via methane decomposition (Eq. 2) and Boudouard reaction (CO disproportionation-Eq. 3) [7]. Another obstacle of DRM is reverse water gas shift reaction (RWGS-Eq. 4), as CO_2 and H_2 both are present in the reaction stream [7,8], and the H_2/CO ratio decreases from the anticipated value for DRM i.e., one. As catalyst design is vital for DRM, it has long been a challenge for researchers to develop a high-performance catalyst to deal with coke deposition and sintering [9].

DRM: $CO_2 + CH_4 \rightarrow 2\,H_2 + 2CO$ ($\Delta H° = +247$ kJ/mol)· (1)

Methane decomposition: $CH_4 \rightarrow 2\,H_2 + C$ ($\Delta H° = +75$ kJ/mol)· (2)

CO disproportionation: $2CO \rightarrow C + CO_2$ ($\Delta H° = -171$ kJ/mol)· (3)

RWGS: $H_2 + CO_2 \rightarrow H_2O + CO$ ($\Delta H° = 41$ kJ/mol)· (4)

Over the last two decades, a large number of catalysts based on noble

---

metals (Pt, Rh, Ru, Ir) and non-noble metals (Ni, Co, Fe) have been explored for DRM, where noble metals-based catalysts have been found to be more prone to resist against coke and sintering than non-noble metal-based catalysts [8,10]. However, the high cost and low abundance of noble metals limited their application. Ni-supported catalysts have drawn considerable attention among transition metals-based catalysts due to their comparable activity to noble metal-based catalysts at initial. Also, it has the potential for industrial applications due to cheaper costs. However, coke and sintering susceptibility of Ni becomes the primary concern for Ni-based catalysts to achieve the desired stability in DRM [11–13]. Therefore, developing a stable Ni-based catalyst is highly desirable for practical industrial applications. This development may be associated with tuning various factors such as electronic metal-support interaction, active metal dispersion, particle size, generating the reactive oxygen species by creating defects, and selecting active metals, promoters and supports [14,15].

In recent years, bimetallic catalyst systems have also drawn a lot of interest in reforming reactions due to their tailored electrical and structural characteristics [12,16,17]. The coke resistivity of noble metals makes them an ideal choice to be incorporated with nickel-based catalysts for reforming reactions [17]. Addition of noble metals alters the redox properties of non-noble metals by keeping them in metallic form by hydrogen spill over [18,19]. An earlier study found that the coke resistivity order in DRM at 500 °C is Pt ~ Pd < Ir = Ru < Rh [20]. Therefore, a combination of Pt and Ni might be a suitable approach towards DRM between the trade-off of high cost and stability of the catalyst [17,19,21], as Pt has remarkable anti-coking properties and Ni is highly active and cheap. For instance, Daniel G. Araiza and his group reported that the bimetallic Pt-Ni/CeO_2 catalyst system showed improved catalytic performance and coke resistivity up to 24 h than the monometallic system [12]. In the Pt-Ni bimetallic system, Pt is beneficial for significantly activating the C-H bond of CH_4 at low temperatures by decreasing the light-off temperature of CH_4, whereas Ni assists the syngas selectivity [22]. V. Palma et al. reported ethanol steam reforming over the Pt-Ni/ supported on CeO_2 with superior activity at 370 °C [18]. J. Niu et al. recently investigated the Pt-Ni system for DRM and observed that the bimetallic system preserved good stability and selectivity by suppressing the RWGS reaction [17].

The current state-of-the-art catalyst designing is not only limited to active metals, but the choice of support also plays a crucial role. In this regard, CeO_2 is a potential candidate to exploit its distinct oxygen mobility, owing to the distinctive Ce^{3+}/Ce^{4+} redox cycle [3,23–26]. Defects chemistry suggests that one oxygen vacancy (V_o) is generated by the reduction of every two Ce^{4+} to Ce^{3+} by the removal of bulk oxygen [27]. These oxygen vacancies on the CeO_2 surface can be filled by the oxygen generated by dissociating CO_2 molecules into O* and CO*, which enhances the catalyst lifespan by preventing coke deposition during DRM [27,28]. Extrinsic defects caused by the insertion of lower valance metal ions (Sm^{3+}, Ni^{2+}, Pr^{3+}, Gd^{3+}) and smaller cations (Si^{4+}, Zr^{4+}) within the host ceria matrix can produce more oxygen vacancies (V_o) due to lattice distortion [29]. These defects and oxygen vacancies (V_o) are not only beneficial to preventing coke deposition by increasing the oxygen ion mobility but are also involved in the low-temperature activity of the catalyst [19,23,30].

The incorporation of lower valance metal cations into the ceria lattice not only generates oxygen vacancies but also enhances metal support interaction by modifying the physical and electronic properties of parent oxides [19,30]. Recently, we have reported partial oxidation of methane at low temperatures over the defect-rich Ni-Pt/CeO_2, which is attributed to the higher oxygen vacancies and strong metal-support interaction (SMSI). [19]. Sagar et al. studied that the Ni(5 wt%)+Cu (15 wt%)/CeO_2 showed good performance and coke resistivity in DRM, which is linked to the formation of Ni-Ce-O solid solution and a high abundance of oxygen vacancies [31]. Kang et al. demonstrated hydrogen production from hydrazine hydrate over the Ni/CeO_2 catalyst synthesized by the combustion method. They claimed that the catalyst

exhibited excellent activity and 100% selectivity of H_2 at 50 °C due to the altered physicochemical properties by forming Ni-Ce-O solid solution [32]. Sk. Mahammadunnisa performed CO oxidation over $NiO/Ce_{1x}Ni_xO_{2-\delta}$ catalyst and claimed that the catalyst works as an alternative to noble metal catalysts owing to enhanced metal dispersion, metal-support interaction and oxygen vacancies resulting from solid solution [33].

Low-temperature DRM could reduce cost and make it more feasible from the industrial point of view. Therefore, current state-of-art catalyst designing is devoted to low-temperature DRM [34,35]. A high abundance of mobile oxygen/oxygen vacancies (V_o) and SMSI could make this task more feasible to achieve. For instance, low-temperature DRM over the Ni-CeO_2/SBA15 catalyst was reported by Yang et al. [36]. They found that the addition of glycine during synthesis increases the extent of $Ni_xCe_{1-x}O_y$ solid solution, resulting in an increment in the Ce^{3+} content from 31% to 49%. The amount of Ce^{3+} content directly links to the amount of oxygen vacancies [36]. Recently, Shen et al. reported low-temperature (300–450 °C) DRM over the defects-rich Pt/CeO_2 catalyst, which is accelerated by the formation of more facile oxygen vacancies (V_o) [23].

The current study aimed to develop a stable catalyst for low-temperature DRM with superior activity. Herein, we establish a simple and one-pot complex combustion technique for the synthesis of a defect-rich Ni-Pt/CeO_2 catalyst. A conventional catalyst was also prepared by the impregnation on commercial CeO_2 support for comparison purposes. To the best of our knowledge, this is the first report on low-temperature DRM with ~86% conversion of CH_4 and CO_2 with 100% selectivity of syngas. The significant role of oxygen vacancies, active oxygen species, Ce^{3+} content, interaction between components, dispersion, particle size, reducibility, and surface area were discussed in detail. This work aims to provide a better understanding of the key factors that should be considered when designing an industrial DRM catalyst.

2. Experimental

2.1. Catalyst synthesis

The materials used are listed in supporting information (SI-S1.1). The catalyst was synthesized by modifying our previously reported solution combustion method in which citric acid monohydrate (CA) was used as a complexing agent and fuel [19]. First, citric acid monohydrate (CA) was dissolved in 15 mL of DI water in a beaker. The required amount of ($Ce(NO_3)_3.6H_2O$), ($Pt(NH_3)_4(NO_3)_2$), and ($Ni(NO_3)_2.6H_2O$) precursors based on catalyst compositions were dissolved in 10 mL of DI water in another beaker, which was then added dropwise to the CA solution and stirred at 40 °C for 1 h. After 1 h, the pH of the entire solution was then adjusted to ~3 by using nitric acid with continuous stirring. Then, 0.25 g of glycine was added to the above solution. The stoichiometric ratio of fuel to metal salts is 1.5. The above solution was then dispersed with 50 mL of ethanol, and the whole mixture was then slowly heated at 60 °C for 4 h to evaporate the ethanol and excess water. After drying the solution at 60 °C with continuous stirring, it was gradually heated to 80 °C until it became a spongy solid. Once the material turns into a spongy semi-solid, the resultant semi-solid transfer to another hot plate preheated at 180 °C. The combustion of a spongy semi-solid with an increase in temperature and the evolution of gases occurred a short time later due to the exothermic reaction between glycine, CA, and metal precursors. After cooling to room temperature, the resultant catalyst was crushed into a fine powder and then calcined in the presence of air at 700 °C for 4 h with a ramping rate of 1 °C/min to get the final catalyst. The final catalysts are denoted as 1NP/CeO_2 (1 wt % Ni-0.5 wt% Pt/CeO_2), 2NP/CeO_2 (2 wt% Ni-0.5 wt% Pt/CeO_2) and 4NP/CeO_2 (4 wt%Ni-0.5 wt% Pt/CeO_2).

We have also synthesized a conventional catalyst by impregnating 2 wt% Ni and 0.5 wt% Pt over the commercial CeO_2 support. For the conventional catalyst, 1 g of CeO_2 support was dispersed into a 50 mL

(50%wt/wt.) water and ethanol solution. Meanwhile, 90 mg of Ni $(NO_3)_2$.6 H_2O and 9.92 mg of $Pt(NH_3)_4(NO_3)_2$ were dissolved in 10 mL of distilled water to make a clear solution. After that, this clear solution was added dropwise to the CeO_2 mixture under continuous stirring at room temperature. After 3 h of stirring at room temperature, the resultant mixture was dried at 80 °C and calcined at 700 °C for 4 h with a ramping rate of 1 °C/min. The final catalyst is denoted as $2NP/CeO_2^{imp}$.

2.2. Catalyst characterization

Synthesized catalysts were characterized thoroughly by X-ray diffraction (XRD), surface area analyzer, scanning electron microscopy (SEM), H_2 temperature-programmed reduction (H_2-TPR), high-resolution transmission electron microscopy (HR-TEM), X-ray photo-electron spectroscopy (XPS), CO pulse-chemisorption, O_2 temperature-programmed desorption (O_2-TPD), CH_4/CO_2 temperature-programmed desorption (CO_2/CH_4-TPD), CH_4 temperature-programmed surface reaction (CH_4-TPSR), Raman, in-situ Raman, thermogravimetry analysis
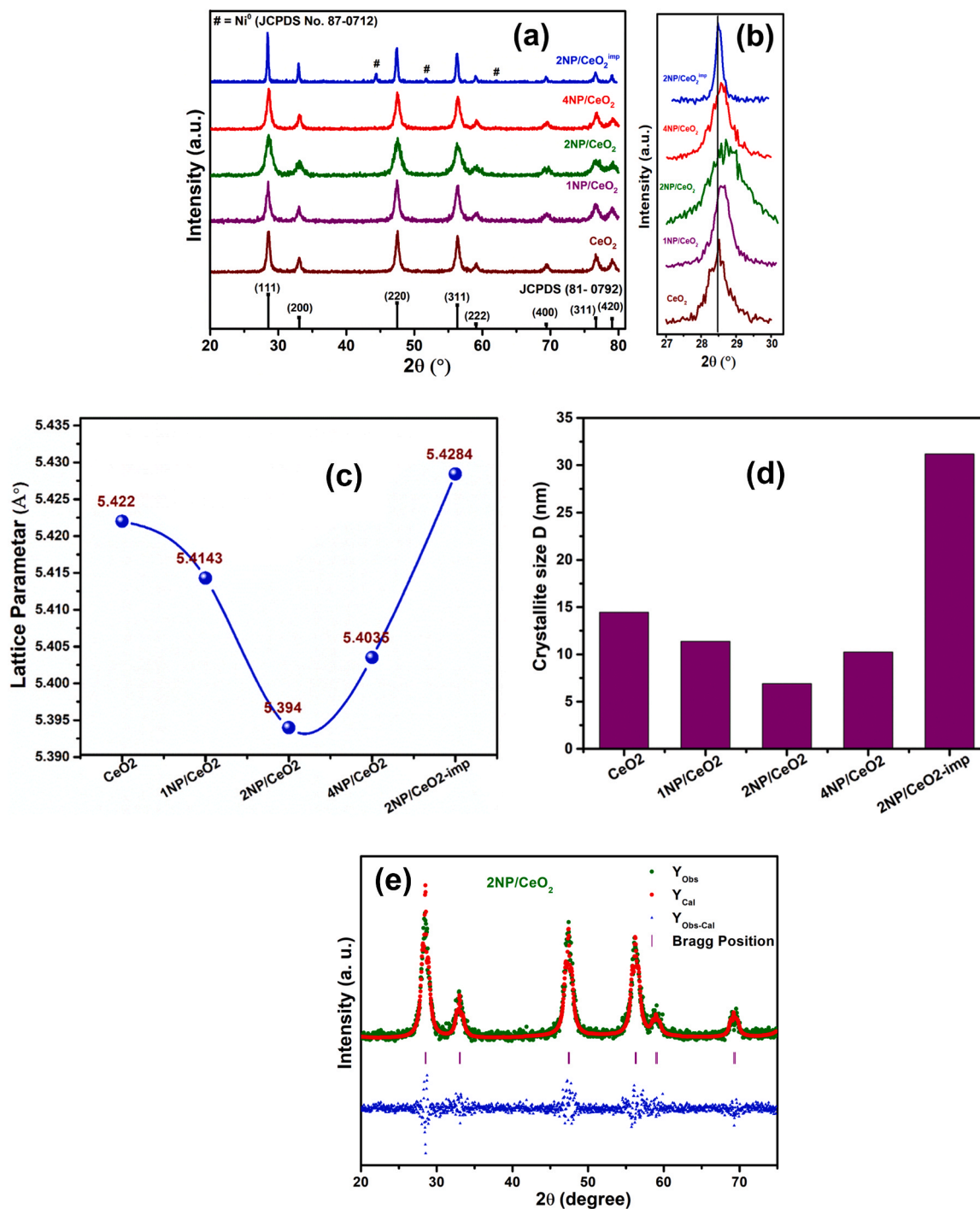

Fig. 1. Powder XRD diffractograms of reduced catalysts (a), 2θ shifting corresponding to the (111) plane (b), change in the lattice parameter (c), crystallite size determined by Scherrer equation corresponding to (111) plane of CeO_2 (d), and Rietveld refinement XRD pattern of $2NP/CeO_2$ catalyst (e). Where, Y_{obs} - observed intensity, Y_{cal} - calculate intensity, $Y_{obs-cal}$ - difference between observed and calculated intensities and vertical lines represent peak position and difference.

(TGA), electron paramagnetic resonance analysis (EPR) and in-situ DRIFT. The details of characterization techniques and procedures, including the DFT method, are given in supporting information.

2.3. Catalysts evaluation

All the experiments for catalysts evaluation were performed in a fixed bed down flow reactor at atmospheric pressure. A detailed procedure is provided in the supporting information (SI).

Following equations have been used to find out the conversion (Eqs. 5–6), product selectivity (Eqs. 7–8), syngas ratio (Eq. 9), and carbon balance (Eq. 10), respectively. A detailed carbon balance was performed for each experiment, and the result was between 98% and 102%.

$$X_{CH_4}(\%) = \frac{(n_{CH_4\ in} - n_{CH_4\ out})}{n_{CH_4\ in}} \times 100 \tag{5}$$

$$X_{CO_2}(\%) = \frac{(n_{CO_2\ in} - n_{CO_2\ out})}{n_{CO_2\ in}} \times 100 \tag{6}$$

$$S_{H_2}(\%) = \frac{n_{H_2\ out}}{2n(CH_4)_{in}} \times 100 \tag{7}$$

$$S_{CO}(\%) = \frac{n_{CO\ out}}{n_{CH_4\ in} + n_{CO_2\ in}} \times 100 \tag{8}$$

$$\frac{H_2}{CO} = \frac{nH_2\ out}{n_{CO\ out}} \tag{9}$$

$$Carbon\ balance\ (\%) = \frac{n_{CH_4\ out} + n_{CO_2\ out} + n_{CO\ out}}{n_{CH_4\ in} + n_{CO_2\ in}} \tag{10}$$

Where X_{CO_2} and X_{CH_4} are the conversion of carbon dioxide and methane in percentage. $n_{z\ in}$ and $n_{z\ out}$ are outlet and inlet molar flow of z (z = CH_4, CO_2, H_2, and CO).

3. Results and discussion

3.1. Catalyst structural and textural analysis

The wide-angle X-ray diffraction (XRD) patterns (2θ range 20–80°) of reduced samples are exhibited in Fig. 1a. All the samples exhibited characteristic peaks of cubic fluorite structure (Fm3m) of CeO_2, which exactly matches with the JCPDS no. 81–0792 [31,37]. The Ni and Pt species are not visible in XRD diffractograms of catalysts synthesized by the solution combustion method. Whereas, in the XRD pattern of conventional catalyst (2NP/CeO$_2^{imp}$), three additional peaks at 2θ values of 44.496°, 51.849° and 76.381° can be seen, which correspond to metallic Ni^0 (JCPDS no. 81–0712). The crystallite size of Ni^0 in 2NP/CeO$_2^{imp}$ was calculated as 27 nm by the Scherrer equation (Table 1). The absence of Ni and Pt species diffraction peaks in 1NP/CeO$_2$, 2NP/CeO$_2$, and 4NP/CeO$_2$ catalysts is most likely due to small particle size and high metal dispersion [19,23]. The literature report suggests that the metal nanoparticles with a size below 5 nm have limitations to detect by XRD

analysis [38]. Furthermore, a noticeable peak broadening for all the catalysts except conventionally impregnated catalyst has been noticed, indicating lattice distortion resulting from incorporating Ni and Pt cations into host ceria lattice [39]. Fig. 1b shows the expanded XRD diffraction corresponding to the (111) plane of cubic fluorite CeO_2. From Fig. 1b, a slight shifting in 2θ Bragg angle towards the higher 2θ side has been observed in 1NP/CeO$_2$, 2NP/CeO$_2$, and 4NP/CeO$_2$ catalysts, indicating lattice contraction resulting from the difference in ionic radii [19,40,41]. On the other hand, this type of shifting towards a higher Bragg angle was not observed in conventional 2NP/CeO$_2^{imp}$ catalyst, confirming there is no solid-solution formation taking place in the impregnated catalyst.

Fig. 1c displayed the change in the lattice parameter of synthesized catalysts with respect to the (111) plane of cubic fluorite CeO_2. The lattice parameters of synthesized 1NP/CeO$_2$ (5.4143 Å), 2NP/CeO$_2$ (5.394 Å), and 4NP/CeO$_2$ (5.4035 Å) catalysts are smaller than undoped CeO_2 (5.422 Å), showing lattice contraction. Formation of $M_xCe_{1-x}O_{2-Y}$ solid solution (where M = Ni and Pt) takes place as the radius of Ni^{2+} (83 pm) and Pt$^{2+/4+}$ (74/76 pm) ions are smaller than the radius of Ce^{4+} (101 pm) [19,31,41,42]. The incorporation of Ni resulted in a continuous decrease in the lattice parameter up to 2% loading of Ni. Afterwards, the value of the lattice parameter slightly increased, suggesting low Ni loading is more favourable for solid solution formation [31,32]. On the other hand, the lattice parameter for the conventional 2NP/CeO$_2^{imp}$ catalyst was the same, confirming that Ni and Pt species are present on the surface of CeO_2 rather than going inside the CeO_2 lattice. Fig. 1d displayed the crystallite size (D) of all the samples. The crystallite size of undoped ceria is 14.5 nm, which decreases as the lattice parameter decreases after doping [43–45]. The 2NP/CeO$_2$ catalyst shows the smallest crystallite size (6.9 nm) as well as the lattice parameter (5.394 Å). A detailed description of a structural feature corresponding to the (111) plane of the cubic fluorite lattice of CeO_2 is given in Table 1. Furthermore, Fig. 1e displayed the Rietveld refinement XRD pattern of the 2NP/CeO$_2$ catalyst. The goodness-of-fit parameters are found to be R_{Bragg} = 8.60, R_F = 5.6, and $χ^2$ = 1.36. The obtained low values of goodness-of-fit $χ^2 = R_{wp}/R_{exp}$ indicated excellent agreement between the refined models and obtained data. The evaluation of the lattice constants for the 2NP/CeO$_2$ catalyst was accomplished by the PROZSKI program. A drop in lattice constant from 5.442 Å (undoped CeO_2) to 5.394 Å (2NP/CeO$_2$) confirms the insertion of Ni and Pt in the CeO_2 lattice.

The XRD patterns of spent catalysts are shown in Fig. S1, and the diffraction patterns of spent 1NP/CeO$_2$ and 2NP/CeO$_2$ catalysts are identical to those of fresh catalysts, indicating that the crystalline phase of incorporated ceria is stable during DRM reaction. On the other hand, 4NP/CeO$_2$ catalyst shows a small diffraction peak at 44.5°, corresponding to the metallic nickel, indicating that the Ni nanoparticles get agglomerated when Ni loading is high (4%). The X-ray diffraction pattern of spent 2NP/CeO$_2^{imp}$ catalyst clearly showed the diffraction peaks correspond to the graphitic carbon at 26.4° [46] and metallic Ni at 2θ values of 44.5° and 51.9° (JCPDS no. 87–0712), which is associated to coke deposition and sintering of Ni nanoparticles on the surface of the catalyst [47].

SEM (Scanning electron microscopy) images of freshly reduced 2NP/CO$_2$ catalyst (at 500 °C) are displayed in Fig. S2, which revealed a sponge-like morphology with surface voids. These voids form due to the excessive volume of gases evolved during combustion and prevent agglomeration within catalysts by forming a porous network [48]. Fig. 2 (a-e) shows the HR-TEM (high-resolution transmission electron microscopy) images of reduced 2NP/CeO$_2$ catalyst, showing a layered structure (Figs. 2a and 2b) in which irregular CeO_2 nanoparticles are closely in contact with each other. The Ni and Pt nanoparticles are almost spherical in shape with an average diameter of 1.5 nm (see the histogram in Fig. 2c) and are uniformly distributed. HR-TEM analysis (Figs. 2d and 2e) revealed that the lattice fringes are separated by d-spacings of 0.223 and 0.207 nm, which correspond to (111) planes of

Table 1
Lattice parameter and crystallite size of the catalysts corresponding to (111) plane.

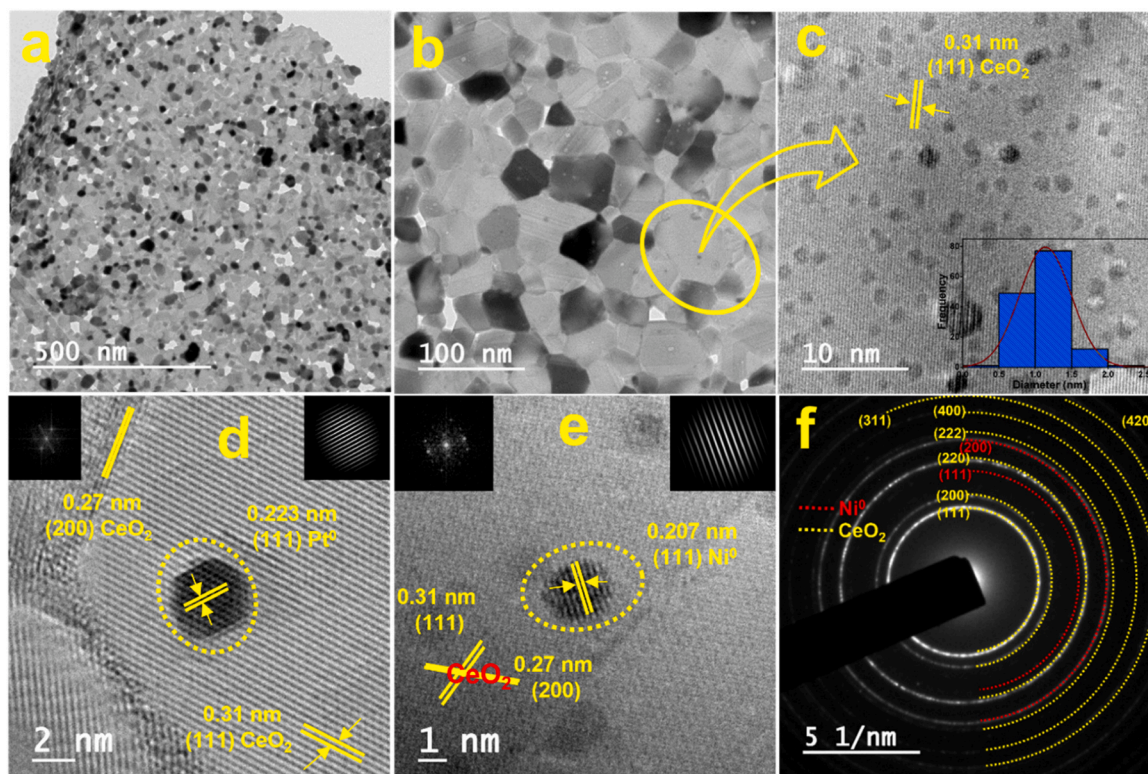| S. No.	Catalyst	Peak Position (θ)	FWHM	Lattice Parameter (Å)	Crystallite Size (nm)	
					CeO$_2$	Ni^0
1	CeO$_2$	28.49	0.5609	5.422	14.5	-
2	1NP/CeO$_2$	28.53	0.7821	5.4143	10.4	-
3	2NP/CeO$_2$	28.64	1.1820	5.394	6.9	-
4	4NP/CeO$_2$	28.59	0.71308	5.4035	11.4	-
5	2NP/CeO$_2^{imp}$	28.46	0.2599	5.4284	31.2	27

Fig. 2. TEM/HR-TEM images at low (a and b) and high magnifications (c-e) of reduced 2NP/CeO$_2$ catalyst. Fig. (2f) represents the SAED pattern 2NP/CeO$_2$ catalyst.

Pt^0 and Ni^0, respectively, confirming the crystalline nature of Pt and Ni species. FFT (left) and inverse FFT (right) of the (111) plane of Pt and Ni nanoparticles are also shown in the inset of Figs. (2d) and (2e), respectively. Lattice fringes of ceria are separated with d-spacings of 0.31 nm (Figs. 2c and 2d), which is due to the (111) plane of CeO$_2$. Additionally, the lattice fringes (d-spacing of 0.27 nm) corresponding to the (200) planes of ceria were also observed (Figs. 2d and 2e). Furthermore, the SAED pattern also confirmed the crystalline nature of Ni species having (111) plane and the fluorite cubic phase of ceria, as illustrated in Fig. 2f. Due to the low loading (0.5 wt%) and high dispersion of Pt, the planes corresponding to Pt are invisible in SAED patterns. The TEM analysis of the 2NP/CeO$_2^{imp}$ catalyst was also carried out and shown in Fig. S3 (supporting information). The 2NP/CeO$_2^{imp}$ catalyst shows an agglomerated morphology, where Ni and Pt species

accumulate over the CeO$_2$ surface and are very big in size.

Fig. 3 shows the EDX spectrum and element mapping of the 2NP/CeO$_2$ catalyst obtained from TEM analysis, validating the presence of Pt, Ni, O and Ce only without any other impurities as well as the uniform distribution of all the elements.

The surface area (SA) of all fresh synthesized samples has been depicted in Table S1 (supporting information). The SA of undoped CeO$_2$ catalyst was estimated to be 65 m^2/g and decreases as Ni loading increases from 1% to 4% in the following trend: 1NP/CeO$_2$ (57 m^2/g) > 2NP/CeO$_2$ (51 m^2/g) > 4NP/CeO$_2$ (39 m^2/g). It has been noted that the decrease in SA is minimal when Ni loading is below 2%, and above 2% Ni loading, surface area decreases sharply. The decrease in surface area could be due to the pore blocking by Ni nanoparticles [31]. The 2NP/CeO$_2^{imp}$ sample showed the lowest value of SA (13 m^2/g),
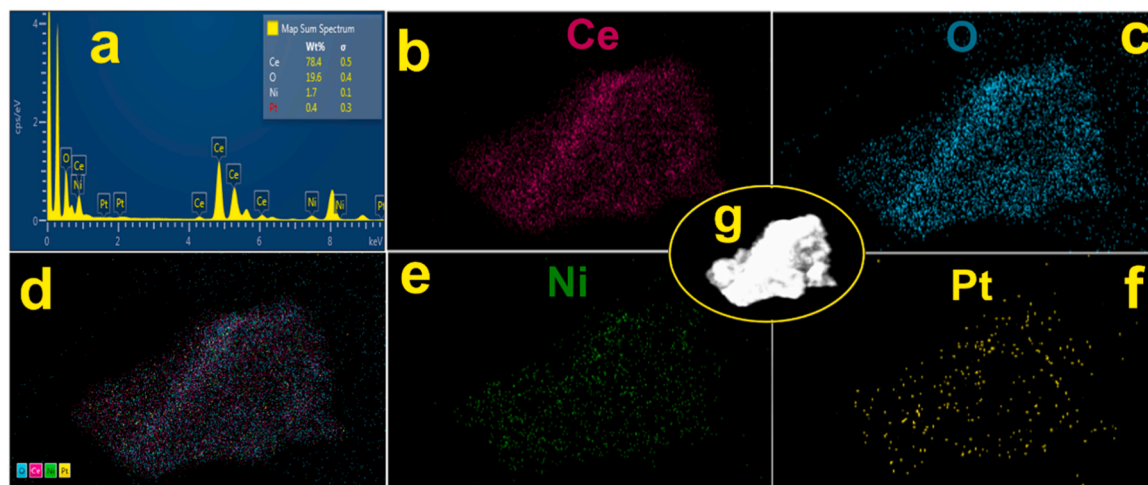

Fig. 3. EDX Spectrum (a), elemental mapping (b-f), and corresponding electron image (g) of reduced 2NP/CeO$_2$ catalyst by TEM analysis.

indicating the blocking of pores as well as the blocking of active CeO_2 surface by agglomeration of metal particles on CeO_2 surface rather than going inside the ceria lattice, as illustrated by TEM analysis. Furthermore, the lowest decrease in SA of spent $1NP/CeO_2$ and $2NP/CeO_2$ catalysts indicates good thermal stability. On the other hand, $2NP/CeO_2^{imp}$ catalyst showed almost 70% decrease in SA after 30 h of reaction. The elemental composition of catalysts is provided in Table S1, which shows that the elemental composition is nearly the same as the input values. All the combustion catalysts exhibited high metal dispersion, and this value decreases as the Ni loading increases $1NP/CeO_2$ (67.2%) > $2NP/CeO_2$ (63.7%) > $4NP/CeO_2$ (47.5%). However, conventional $2NP/CeO_2^{imp}$ catalyst exhibited the lowest value of metal dispersion (9.6%) due to the accumulation of Ni nanoparticles over the CeO_2 support (Table S1). The catalyst synthesized by the solution combustion method showed higher values of metal dispersion due to the formation of smaller metal nanoparticles [49].

Using H_2 temperature-programmed reduction (H_2-TPR), as illustrated in Fig. 4, the reducibility and metal-support interactions of fresh catalysts were investigated. Table S2 provides the total H_2 consumption for all catalysts. Reduction of outlying surface oxygen on synthesized CeO_2 support begins to consume H_2 below 100 °C and continuous up to around 500 °C, indicating the presence of a good abundance of readily available surface oxygen species that are reducible at such a low temperature [19]. Furthermore, the H_2 consumption of bulk oxygen results in a broad reduction peak (δ) at higher temperatures with T_{max} at 760 °C [50]. The reduction profile of $1NP/CeO_2$, $2NP/CeO_2$, and $4NP/CeO_2$ samples showed similar type of H_2-TPR patterns. The reduction patterns can be divided into four peaks (α, β, γ and δ). It is evident from Fig. 4 that the H_2 consumption for reactive oxygen species begins at 120 °C and continues to 350–400 °C, where three shoulder peaks, α, β, and γ can be seen. First broad peak, designated as α, is associated with the reduction of reactive oxygen species adsorbed at oxygen vacancies resulting from the formation of $M_xCe_{1-x}O_{2-Y}$ (M = Ni, Pt) solid solution [50]. When Ce^{4+} is replaced by Ni and Pt ions, charge imbalance and lattice distortion occur, which generates more oxygen vacancies (V_o). These V_o sites can store oxygen in various forms, such as peroxide and superoxide (O_2^{2-}, O_2^-), which are highly active [50,51] and can be reduced at low temperatures [32,50]. However, this α peak was not observed for the $2NP/CeO_2^{imp}$ catalyst, suggesting no solid solution formation occurs within the $2NP/CeO_2^{imp}$ catalyst. The second shoulder peak designated as β, appearing in the 210–250 °C range, could be due to the reduction of oxygen vacancies [32,51,52] and highly dispersed PtO_x nanoparticles [53]. Furthermore, the third broad peak (γ) within 240–400 °C, T_{max} at 292, 307 and 303 °C for $1NP/CeO_2$, $2NP/CeO_2$ and $4NP/CeO_2$ could be ascribed due to H_2 consumption for the oxygen vacancies on Ni-Ce

Fig. 4. H_2-TPR patterns of fresh catalysts.

interface and NiO species having strong metal-support interaction [19]. Previous research has shown that the reduction of incorporated Ni is difficult. Therefore, the broad reduction pattern shows higher H_2 consumption, which could be related to the reactive oxygen species engendered on the Ni-Ce interface and NiO_x species having strong interaction with CeO_2 [36]. The higher temperature peaks (δ) at about 780 °C are attributed to the H_2 consumption for bulk oxygen.

It has been observed that there is a clear difference in the reduction pattern of conventional catalyst and the catalysts synthesized by the combustion method (Fig. 4). Conventional catalyst showed only three peaks, the first and second peaks at 132 and 270 °C, are associated with the reduction of weakly interacting PtO_x and NiO aggregates on CeO_2 surface, respectively. As shown in Fig. 4 and Table S2, H_2 consumption for bulk oxygen is higher in $2NP/CeO_2^{imp}$ compared to $1NP/CeO_2$, $2NP/CeO_2$ and $4NP/CeO_2$ catalysts, implying that $2NP/CeO_2^{imp}$ has more bulk oxygen, while catalysts synthesized by combustion method have more surface oxygen. Furthermore, when the H_2 consumption (100–450 °C) of $2NP/CeO_2$ and $2NP/CeO_2^{imp}$ catalysts (with similar loading) is compared, it is clear that the $2NP/CeO_2$ catalyst has more surface oxygen species than the conventional catalyst. These surface oxygen species (O_2^{2-}, O_2^-) are beneficial to low-temperature activation of CO_2 and CH_4 molecules and coke inhibition during reaction.

3.2. Defect sites and electronic environment of the active center

The electronic speciation and chemical state of Pt, Ni, O, and Ce were analyzed by the XPS (X-ray photoelectron spectroscopy) analysis of reduced samples. Figs. 5a and 5b show deconvoluted Pt 4f and Ni 2p core level XPS spectra of $2NP/CeO_2$ catalyst. The presence of Pt^0 (71.1 and 74.7 eV) and Pt^{2+} (72.6 and 76 eV) states can be seen in deconvoluted XPS spectra of Pt 4 f (Fig. 5a) [19,23,42]. The extended form of Ni 2p XPS spectra displayed the presence of Ni in its metallic Ni and Ni^{2+} state with different surrounding environments, where Ni^{2+} state is more pronounced. The peak at 852.8 eV corresponds to metallic Ni, while peaks at 855.8 and 858.6 eV correspond to Ni^{2+} states with octahedral (Ni_{OC}^{2+}) and tetrahedral (Ni_T^{2+}) arrangements, respectively [19,54,55]. The stated value of the binding energy for Ni^{2+} is relatively higher than the reported for free NiO (854.2 eV), which may be due to the strong Ni-Ce-O bonding [54].

Fig. 6 displayed the deconvoluted Ce 3d XPS spectra of all catalysts. The presence of Ce^{3+} and Ce^{4+} ions on the catalyst surface can be determined by the spin-orbital splitting of $3d_{5/2}$ and $3d_{3/2}$ [56,57]. The spectra can be deconvoluted into 10 peaks attributed to $3d_{3/2}$ and $3d_{5/2}$ components [58]. In which four peaks denoted as α, α'', β, and β'' at the binding energies of 881.3, 885.2, 900, and 903.4 eV, respectively, are characteristics of Ce^{3+} ions ($3d^{10}4 f^1$ initial electronic state), whereas remaining six peaks denoted as α', α''', α'''', β', β''', and β'''' are characteristics of Ce^{4+} ions (($3d^{10}4 f^0$ initial electronic state) [19,56]. According to Wang et al., a positive shift (a shift towards higher binding energy) in the binding energy of the $3d_{5/2}$ component of ceria is associated with Ni-Ce-O interaction [59]. A similar positive shift in Ce $3d_{5/2}$ component can be seen in our prepared catalyst (except $2NP/CeO_2^{imp}$), which is the maximum for $2NP/CeO_2$ (883.1 eV) followed by $1NP/CeO_2$ (882.9 eV) > and $4NP/CeO_2$ (882.8 eV). The surface concentrations of Ce^{3+} and Ce^{4+} were determined by using the following equations (Eqs. 11 and 12) and given in Table 2.

$$Ce^{3+}(\%) = \frac{[a(Ce^{3+})]}{[a(Ce^{3+}) + a(Ce^{4+})]} \times 100 \qquad (11)$$

$$Ce^{4+}(\%) = \frac{[a(Ce^{4+})]}{[a(Ce^{3+}) + a(Ce^{4+})]} \times 100 \qquad (12)$$

Where, $a(Ce^{3+})$ and $a(Ce^{4+})$ are the total integrated areas of peaks corresponding to Ce^{3+} and Ce^{4+}, respectively. The proportion of Ce^{3+} decreases in the order: $2NP/CeO_2$ > $4NP/CeO_2$ > $1NP/CeO_2$ >> 2NP/
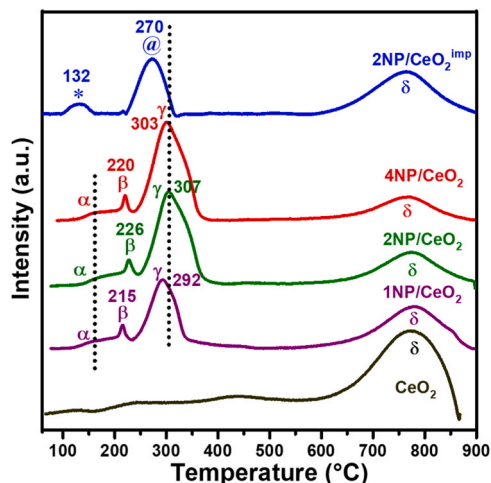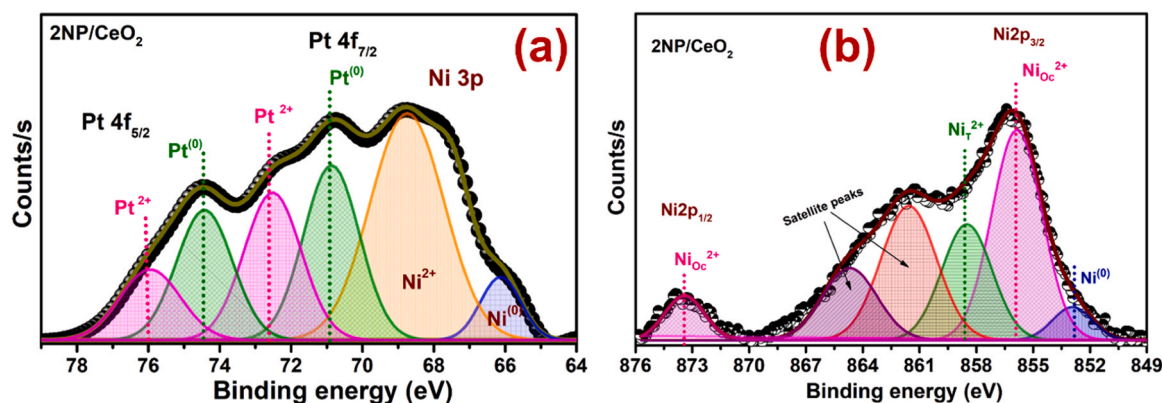
Fig. 5. XPS spectra of Pt 4 f (a), and Ni 2p (b) of reduced 2NP/CeO$_2$ catalyst.
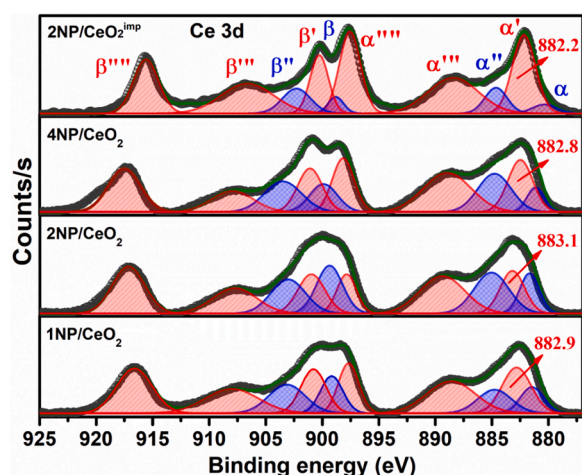
Fig. 6. XPS spectra of Ce 3d of reduced 1NP/CeO$_2$, 2NP/CeO$_2$, 4NP/CeO$_2$ and 2NP/CeO$_2^{imp}$ catalysts.

Fig. 7. XPS spectra of O 1s of 1NP/CeO$_2$, 2NP/CeO$_2$, 4NP/CeO$_2$ and 2NP/CeO$_2^{imp}$ catalysts.

Table 2
Ce^{3+}, Ce^{4+} and oxygen species ratio calculated from XPS data.

Catalyst	Ceria		Oxygen		
	Ce^{3+}	Ce^{4+}	O$_L$	O$_V$	O$_V$/O$_V$+O$_L$
1NP/CeO$_2$	22.8	77.2	59.5	40.5	0.40
2NP/CeO$_2$	32.4	67.6	49	51	0.51
4NP/CeO$_2$	26.2	73.8	56	44	0.44
2NP/CeO$_2^{imp}$	14.2	85.8	87.5	12.5	0.12

CeO$_2^{imp}$. The Ce^{3+} concentration is associated with the number of oxygen vacancies, which can be produced by reducing Ce^{4+} to Ce^{3+} after incorporating low-valent metal cations [30,54].

Fig. 7 displayed the deconvoluted O 1s XPS spectra of all the prepared catalysts, where two types of surface oxygen species can be seen. The peaks at 529.1 eV (O$_L$) and 531.2 eV (O$_V$) are ascribed to the lattice oxygen and oxygen vacancies (O$_V$), respectively [19,60–62]. According to previous studies, the inclusion of low-valent metal cations within ceria lattice leads to charge imbalance and lattice distortion within the ceria lattice. As a result, more oxygen vacancies are generated within the catalyst [32,54]. As a result, highly reactive oxygen species (O$_2^-$ and O$_2^{2-}$) are produced, and these reactive oxygen species are more reactive than the lattice oxygen (O^{2-}), which has a positive impact in preventing coke deposition as well as in low-temperature activation of CO$_2$ and CH$_4$. The formation of superoxide ions was also confirmed by the room temperature EPR, Raman and DRIFT analysis (discussed later). The ratio of reactive oxygen species to total oxygen (O$_V$/O$_V$+O$_L$) was calculated
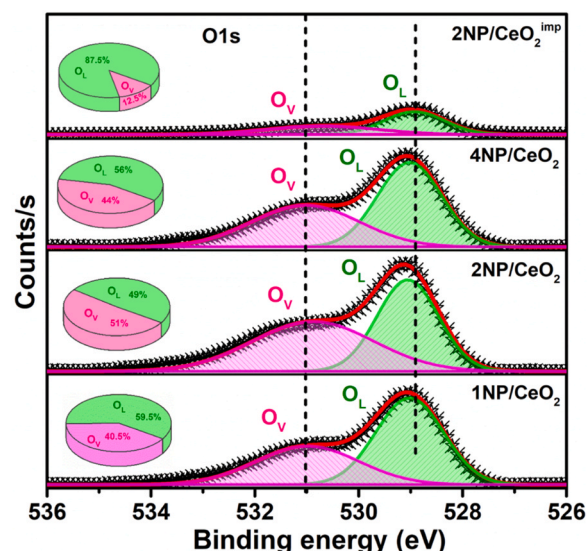
using their integrated areas of the corresponding peaks, as shown in Table 2. The proportion of reactive oxygen species is consistent with the ratio of Ce^{3+} ions. Furthermore, if we compare the intensities of the O 1s spectra (Fig. 7), it can be seen that a very small portion of oxygen species are exposed on the surface of the 2NP/CeO$_2^{imp}$ catalyst. On the other hand, in the case of the catalysts prepared by the solution combustion method, a substantial amount of oxygen species is exposed on the surface. The XPS spectra of Ce, O, Ni and Pt of the spent 2NP/CeO$_2$ catalyst after the 700 h stability test are shown in supporting information (Fig. S4). The XPS spectra of the spent 2NP/CeO$_2$ catalyst showed a slight change after 700 h of reaction, which might be due to the fact that most of the platinum exists in the Pt^0 state, although Pt^{2+} also exists, as confirmed by Fig. S4a. On the other hand, the XPS spectra of Ni 2p do not show any changes. Moreover, the XPS spectra O 1s (Fig. S4c) and Ce 3d (Fig. S4d) showed a slight decrease in the O$_v$ (from 51% to 45%) and Ce^{3+} content (from 32.4% to 29.5%). In addition, the XPS spectra of Ce 3d also showed some changes in the basic spectra, which may be due to an increase in the crystallinity after 700 h of reaction, as confirmed by the XRD pattern of the spent 2NP/CeO$_2$ catalyst (discussed later).

Raman spectroscopy is an effective analytical tool for eliciting additional structural information about defects and lattice distortion within oxide catalysts. Fig. 8a shows the Raman spectra of the reduced catalysts prepared by the solution combustion method by varying Ni loading. All the prepared catalysts exhibited the characteristic Raman
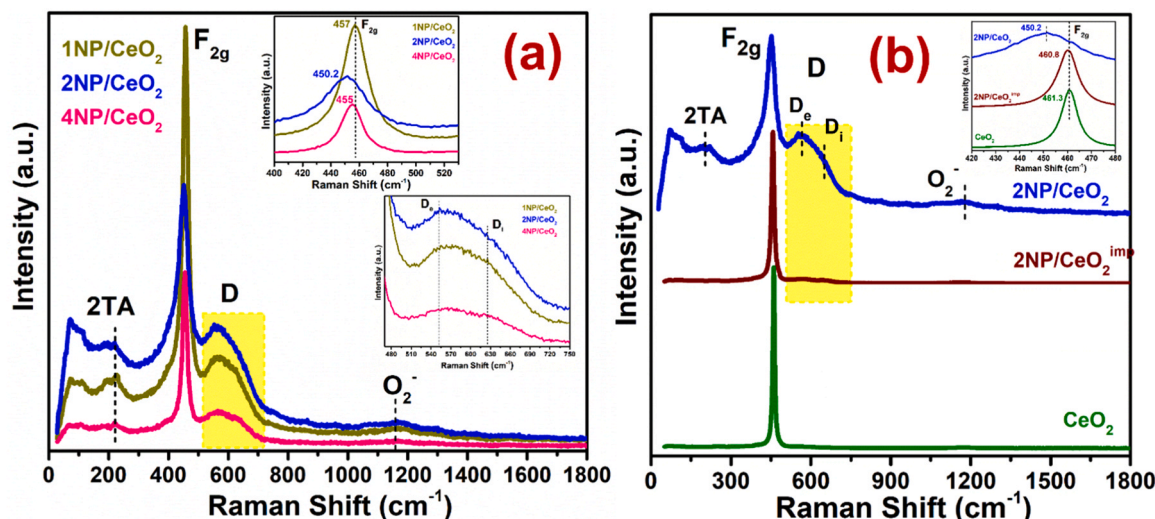
Fig. 8. Raman spectra of reduced 1NP/CeO$_2$, 2NP/CeO$_2$, and 4NP/CeO$_2$ (a), and undoped CeO$_2$, 2NP/CeO$_2$, and 2NP/CeO$_2^{imp}$ catalysts for comparison (b).

active F$_{2g}$ band in between 450-457 cm^{-1}, which is associated with the symmetrical stretching of oxygen atoms surrounding the cation of Ce-O$_8$ unit [19,23,57]. Generally, in pure CeO$_2$, this F$_{2g}$ band appeared at around 460–470 cm^{-1} [63,64]. A redshift (a shift towards lower frequency) was observed for all the catalysts (inset of Fig. 8a), which is associated with the lattice strain and topological defects arising from the incorporation of low valent cations within host CeO$_2$ matrix [63]. Moreover, this red shift is more prominent in 2NP/CeO$_2$ catalysts (450.2 cm^{-1}), and follows the order: 2NP/CeO$_2$ > 4NP/CeO$_2$ > 1NP/CeO$_2$. According to past literature, redshift is directly proportional to the lattice strain and topological disorders [63]. This indicates that the 2NP/CeO$_2$ catalyst have a higher extent of lattice strain and topological disorder. Some literature reported that the redshift is also associated with the smaller crystallite size of CeO$_2$ [63,64]. Indeed, 2NP/CeO$_2$ has the smallest crystallite size (6.9 nm). Moreover, a defective CeO$_2$ lattice structure is further validated by a band at 220 cm^{-1} caused by the doubly degenerate transverse optical (TO) or second-order transverse acoustic (2TA) modes of CeO$_2$ [63,65]. This band is Raman inactive in a perfect CeO$_2$ lattice [63]. The formation of solid solution in combustion catalysts leads to the broadening of the F$_{2g}$ band.

In general, oxygen vacancies are produced in order to maintain overall charge neutrality. Prominent broad peaks at ~500–700 cm^{-1} are the defects-induced bands (D) associated with the formation of oxygen vacancies (V$_o$), which can be classified as extrinsic (D$_e$) and intrinsic defects (D$_i$), as illustrated in the inset of Fig. 8a [29,63]. Extrinsic (D$_e$) and intrinsic (D$_i$) defects at ~560 and ~630 cm^{-1} are associated with the generation of oxygen vacancies in order to maintain charge neutrality when Ce^{4+} is replaced by Ni^{2+}/Pt^{2+} (extrinsic defects) and Ce^{3+} (intrinsic defects), respectively [23,29,56,65,66]. These V$_o$ sites starve to adsorbed oxygen species in a form (O$_2^-$, O$_2^{2-}$) that is highly active. The band at ~1160 cm^{-1} may be due to reactive superoxide species (O$_2^-$) dissociatively adsorbed on the V$_o$ sites [67].

Fig. 8b shows the Raman spectrum of pure CeO$_2$, 2NP/CeO$_2$, and 2NP/CeO$_2^{imp}$ catalysts for comparison. The position of the F$_{2g}$ band in pure CeO$_2$ and 2NP/CeO$_2^{imp}$ catalysts is almost similar, i.e., ~461 cm^{-1}, while the 2NP/CeO$_2$ catalyst showed significant shifting towards the lower side and broadening (450.2 cm^{-1}) in F$_{2g}$ band (inset of Fig. 8b), showing no solid solution formation takes place in 2NP/CeO$_2^{imp}$. The amount of oxygen vacancies was estimated by the A$_D$/A$_{F2g}$ ratio shown in Table S3 (supporting information), which is determined by using the corresponding integrated areas of D (where D = D$_e$ + D$_i$) and the F$_{2g}$ bands [42,57]. A$_D$/A$_{F2g}$ ratio follows the order: 2NP/CeO$_2$ (0.58) > 4NPCeO$_2$ (0.47) > 1NP/CeO$_2$ (0.39) >> 2NP/CeO$_2^{imp}$ (0.086), where

the higher value of A$_D$/A$_{F2g}$ ratio in 2NP/CeO$_2$ catalyst shows the higher concentration of surface oxygen vacancies. The obtained A$_D$/A$_{F2g}$ ratio is consistent with the findings of XRD and XPS analysis.

The oxygen species adsorbed at defect sites are thought to be an important factor for the low-temperature CH$_4$ and CO$_2$ activation and coke-resistant behaviour of the catalyst. To gain a thorough understanding of the characteristics of oxygen sites, O$_2$ temperature-programmed desorption (O$_2$-TPD) of all the samples was performed, as shown in Fig. 9. According to the earlier literature, i) desorption peaks in between 100-250 °C (O$_I$) are associated with weakly bound or superficial oxygen species on the catalyst surface, ii) desorption peaks in between 250-600 °C (O$_{II}$) are generally associated with reactive oxygen species (O$_2^{2-}$, O$_2^-$) bound to the oxygen vacancies (V$_o$), and iii) the afterwards peaks > 600 °C (O$_{III}$) are associated with the lattice oxygen (O^{2-}) [57,66,68]. The reactive oxygen species (O$_2^{2-}$, O$_2^-$) act as active sites for low-temperature activation of CH$_4$ and CO$_2$ and prevent coke deposition [23,30]. It can be seen that the 1NP/CeO$_2$, 2NP/CeO$_2$, and 4NP/CeO$_2$ catalysts show the maximum amount of O$_2$ desorbed in the O$_{II}$ region, while 2NP/CeO$_2^{imp}$ catalyst shows the maximum desorption after 650 °C. These results are well agreed with the TPR data, as 2NP/CeO$_2^{imp}$ catalyst has more bulk oxygen, and the catalysts synthesized by the combustion method have more surface oxygen vacancies. The intensity of desorbed peaks in O$_{II}$ region increases initially when Ni loading increases to 2%, and above 2% loading, intensities decrease. The
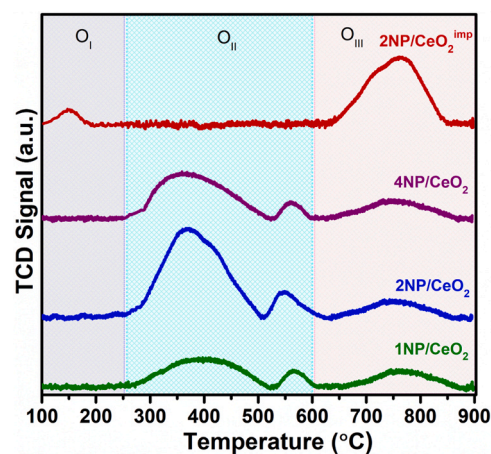

Fig. 9. O$_2$-TPD of fresh 1NP/CeO$_2$, 2NP/CeO$_2$, 4NP/CeO$_2$ and 2NP/CeO$_2^{imp}$ catalysts.

amount of O_2 desorbed per region is calculated by using their corresponding integrated areas and tabulated in Table 3. The number of reactive species (O_{II}) is highest in the 2NPCeO$_2$ catalyst and follows the order: 2NP/CeO$_2$ > 4NP/CeO$_2$ > 1NP/CeO$_2$ > 2NP/CeO$_2^{imp}$. The total amount of desorbed O_2 also marked a similar trend.

3.3. Chemisorption studies

CH$_4$/CO$_2$-TPD (temperature-programmed desorption) are used to investigate the difference in the chemisorption properties of the synthesized catalysts, support and impregnated catalyst. Figs. 10a and 10b show the CO_2 and CH$_4$-TPD patterns of the catalysts. The CO$_2$/CH$_4$ desorption patterns are divided into three regions, weak, moderate and strong, ranging in between 100-250 °C, 250-500 °C and above 500 °C for CO$_2$ -TPD and 50–300 °C, 300–560 °C, above 560 °C for CH$_4$-TPD [23,57,60]. From Fig. 10a, we can see that pure CeO$_2$ does not show any desorption peak of CO$_2$, whereas, in case of 2NP/CeO$_2^{imp}$ catalyst, a small fraction of CO$_2$ adsorption takes place in a weak region. Earlier studies show that increased oxygen vacancies (V_o) may assist the adsorption and activation of CO$_2$ molecules by inserting one oxygen atom into the V_o sites [14,60]. Indeed, in case of the catalysts synthesized by the combustion method, CO$_2$ adsorption increases between weak and moderate regions, which may be associated with the extrinsic defects after incorporating the Pt and Ni species within CeO$_2$ lattice. Literature reports revealed that the weak and moderate sites play a vital role in CO$_2$ adsorption and desorption, followed by product formation, whereas strong sites are not suitable for the stable DRM reaction since strong sites prompt the coke formation [3]. In case of CH$_4$-TPD, pure CeO$_2$ support showed a small amount of adsorption in weak and moderate regions, which might be associated with the oxygen vacancies generated by the Ce^{3+} species. After incorporating the Ni and Pt, CH$_4$ adsorption increases as the A_{F2g}/A_D and O_V/O_V+O_L ratio increases, as estimated by Raman and XPS analysis.

The CO$_2$ adsorption follows the order: 2NP/CeO$_2$ > 4NP/CeO$_2$ > 1NP/CeO$_2$ > 2NP/CeO$_2^{imp}$. The adsorption of CH$_4$ also follows a similar pattern (Table 4) as CO$_2$ and 2NP/CeO$_2$ catalyst showed the maximum CH$_4$ (0.418 cm^3/g) and CO$_2$ (0.98 cm^3/g) adsorption. The obtained trends of CO$_2$/CH$_4$ adsorption are in good agreement with O$_2$-TPD (reactive oxygen species), XPS (O_V/O_V+O_L), and Raman (A_{F2g}/A_D) analysis. The major difference in CH$_4$/CO$_2$-TPD is that in case of CH$_4$-TPD, maximum adsorption takes place in weak regions, whereas, in case of CO$_2$-TPD, maximum adsorption takes place in moderate regions, suggesting that there is a different mechanism for activating of CO$_2$ and CH$_4$ [23] (discussed later by in-situ DRIFT, RAMAN and DFT calculations).

3.4. Investigation of reaction mechanism

To determine the reaction intermediate and elucidate the reaction mechanism, CH$_4$ and CO$_2$ activation over the 2NP/CeO$_2$ catalyst was monitored by in-situ DRIFT at 350 °C. In order to understand the reaction mechanism, the DRIFT spectra were recorded in three steps over the

Table 3
Amount of O_2 desorbed at different temperature ranges.

Catalyst	O_I (100–250 °C) (cm^3/g)	O_{II} (100–600 °C) (cm^3/g)	O_{III} (< 600 °C) (cm^3/g)	Total amount of desorbed O_2 (cm^3/g)
1NP/ CeO$_2$	-	0.254	0.13	0.38
2NP/ CeO$_2$	-	0.532	0.112	0.64
4NP/ CeO$_2$	-	0.373	0.117	0.49
2NP/ CeO$_2^{imp}$	0.031	-	0.31	0.34

2NP/CeO$_2$ catalyst; i) in presence of CH$_4$ after reduction (Fig. S5), ii) in presence of CO$_2$ (Fig. 11), and iii) in presence of CH$_4$ followed by CO$_2$ exposure (Fig. 12). The exposure of CH$_4$ over reduced 2NP/CeO$_2$ sample (Fig. S5) exhibited peaks at ~3016 and 1305 cm^{-1} which are assigned for the gaseous phase of methane [57,69]. No other bands were observed when spectra were recorded in presence of methane on the reduced catalyst. For second step, DRIFT spectra were recorded in presence of CO$_2$ after 30 min of N$_2$ flow (30 mL/min) to remove the gaseous CH$_4$ (Fig. 11). Several bands appeared after the introduction of CO$_2$ in the reaction cell. The bands at 2350 cm^{-1} are attributed to the gaseous CO$_2$ [69,70]. The exposure of CO$_2$ over the 2NP/CeO$_2$ catalyst surface exhibited chemisorbed linear CO at 2085 cm^{-1}, CO$_3^{2-}$, metal carbonates (blue shaded region), O$_2^-$ (1060 cm^{-1}), and O$_2^{2-}$ (856 cm^{-1}) [23,57,69]. The intensity of all the bands increases up to 4 min and afterwards becomes constant, this might be due to the generation of active oxygen species by dissociating CO$_2$ into CO and active oxygen species (O*). Now the CO$_2$ gas was switched to the CH$_4$ and spectra were recorded, as shown in Fig. 12. The exposure of CH$_4$ followed by the CO$_2$ exposure on the 2NP/CeO$_2$ surface resulted in the appearance of chemisorbed CO bands at ~2025 and 2085 cm^{-1} (linearly coordinated at metal sites), CH$_x$O (1162 and 1393 cm^{-1}), superoxide (O$_2^-$) (1060 cm^{-1}), peroxide (O$_2^{2-}$) (856 cm^{-1}) and metal carbonates (blue shaded region) [23,57,69,71]. The bands near 3016 and 1305 cm^{-1} are assigned to the gas phase methane [57]. The intensity of CO, CH$_x$O, O$_2^-$, and O$_2^{2-}$ related peaks decreases as time increases, indicating the consumption of active oxygen species in the presence of CH$_4$. The presence of CH$_x$O, CO, O$_2^-$ and O$_2^{2-}$ species in DRIFT spectra suggested a reactive oxygen species assisted CH$_4$ activation [23].

In-situ DRIFT in presence of feed (CH$_4$/CO$_2$/N$_2$) were performed at 350 °C (Fig. 13). The bands at 1305, 3016 and ~2340 cm^{-1} are attributed to the gaseous phase of CH$_4$ and CO$_2$, respectively, [64,67]. At initial, sequential C-H bond activation takes place over the 2NP/CeO$_2$ surface with the help of Pt [19], then these CH$_x$ species transfer from the platinum to neighbouring active oxygen species (O$_2^-$ and O$_2^{2-}$) to form CH$_x$O intermediate (Fig. 11) [23]. Recently, our study showed that the addition of Pt decreases the C-H bond activation energy of methane by 8 kcal/mol compared to the Ni/CeO$_2$, and the decrease in activation energy resulted from the bond elongation and extra stabilization of the transition state with the help of extra bond of H atom with Pt [19]. Later, the CH$_x$O intermediate dissociates into CO (Fig. 13) rather than inactive carbon with the help of reactive oxygen species. The introduction of the reaction feed mixture into the reaction cell resulted in the chemisorbed CO bands at ~2085 and ~2015 cm^{-1}. The bands observed in the region of 2100–1900 cm^{-1}, are characteristic of linearly coordinated carbonyl at M^0 and M$^{\delta+}$ sites (where M = Pt/Ni) [72,73]. The shoulder band at ~2015 cm^{-1} is due to the linearly coordinated CO on metal sites (M^0) [70,73,74]. Whereas, the intense band at ~2085 is due to the linearly coordinated mono or multiple CO at metal (M$^{\delta+}$) sites (where M = Ni/Pt) [69,73,75]. A small band at ~2180 cm^{-1} was also observed, which is attributed to the gaseous CO in the reaction cell [69]. Furthermore, chemisorbed bands associated with CH$_x$O at 1162, 1386 cm^{-1}, metal carbonates (blue shaded region), superoxide (O$_2^-$) at 1062 cm^{-1} and peroxide (O$_2^{2-}$) at 857 cm^{-1} can be seen. The presence of O$_2^-$ species was also confirmed by the EPR analysis (discussed later). The formation of CH$_x$O intermediate revealed the reactive oxygen species assisted activation of CH$_4$, as a result, oxygen vacancies (V_o) formed, where CO$_2$ get adsorbed on the V_o sites resulting in the generation of reactive oxygen species and linear CO [23,29,60]. The constant intensity of O$_2^-$ and O$_2^{2-}$ bands in the feed mixture firmly supported the consumption and regeneration of active oxygen species taking place during DRM.

In order to get a deep understanding about the structural alteration during DRM reaction, the in-situ Raman study was performed at 350 °C in presence of CH$_4$, CO$_2$, and feed mixture, respectively. We can see that in presence of methane, the intensity of 2TA, F$_{2g}$, and defects-induced D bands decrease gradually as the time increases from 1 to 10 min,

Fig. 10. Chemisorption properties, (a) CO_2-TPD, and (b) CH_4-TPD of fresh 1NP/CeO$_2$, 2NP/CeO$_2$, 4NP/CeO$_2$ and 2NP/CeO$_2^{imp}$ catalysts.

Table 4
distribution of CO_2/CH_4 adsorption sites by CO_2/CH_4 TPD.

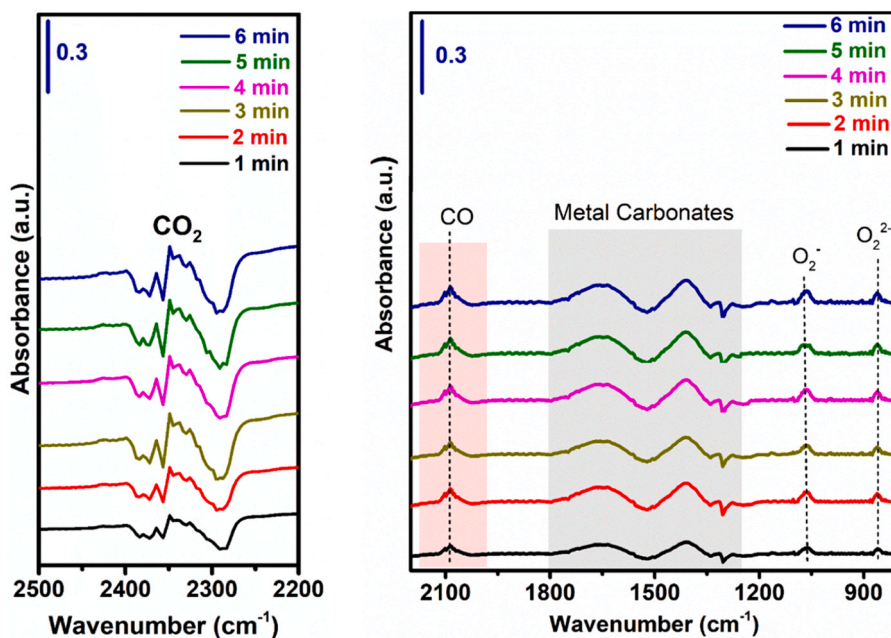| Catalyst	CO_2 TPD			CH_4 TPD		
	I (100–250 °C)	II (251–500 °C)	Total (cm^3/g)	I (100–250 °C)	II (251–500 °C)	Total (cm^3/g)
CeO$_2$	-	-	-	0.033	0.012	0.044
1NP/CeO$_2$	0.052	0.108	0.16	0.33	0.062	0.392
2NP/CeO$_2$	0.137	0.281	0.418	0.68	0.30	0.98
4NP/CeO$_2$	0.066	0.147	0.213	0.46	0.17	0.63
2NP/CeO$_2^{imp}$	0.033	0.013	0.046	0.067	0.021	0.088

Fig. 11. *In-Situ* DRIFT analysis of CO_2 activation over the reduced 2NP/CeO$_2$ catalyst, CO_2 was separately adsorbed at 350 °C for 6 min under 10% CO_2/N_2 flow at 36 mL/min.

afterwards become constant. The peak intensity of the O_2^- species also decreases with time. On the other hand, when Raman spectra were recorded in presence of CO_2, an opposite phenomenon was observed, as illustrated in Fig. 14b. The intensity of O_2^-, 2TA, F_{2g} and defects-induced bands (D) increases gradually as the time increases from 1 to 10 min.

Afterwards, no increase in the intensity was observed. These findings suggest that the consumption of reactive surface oxygen species by CH_4 molecules generates oxygen vacancies (V_o), which promotes the activation of CO_2 [29] and regenerates by dissociating CO_2 into CO and O* [76]. As a result, the intensities of O_2^-, 2TA, F_{2g}, and D bands remain
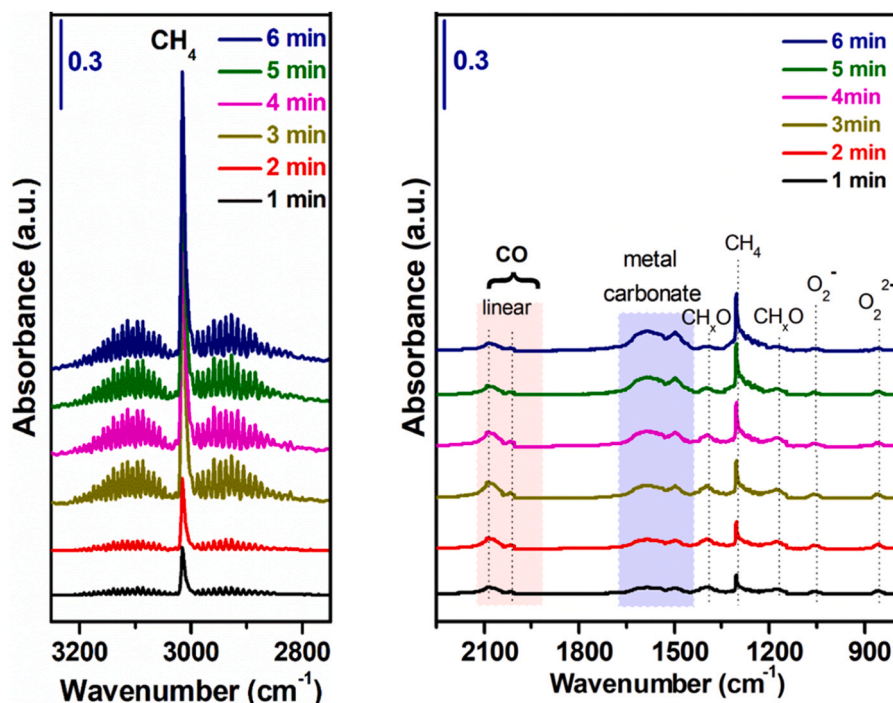
Fig. 12. *In-Situ* DRIFT analysis of CH_4 activation over the $2NP/CeO_2$ catalyst after generating active oxygen species by CO_2 (30 min), then CH_4 was separately adsorbed at 350 °C for 6 min under 10% CH_4/N_2 flow at 36 mL/min.
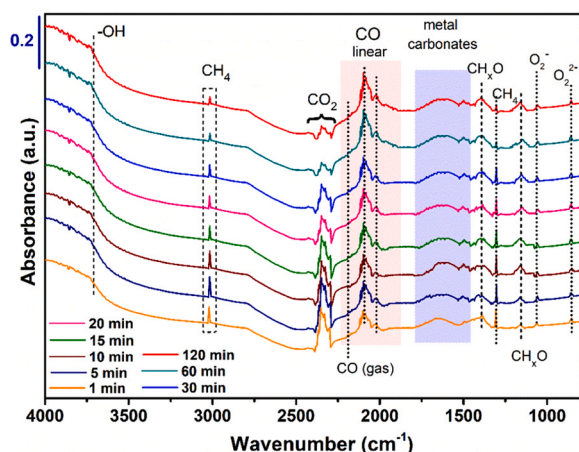

Fig. 13. *In-Situ* DRIFT spectra over the $2NP/CeO_2$ catalyst, (analysis carried out at 350 °C at 1 atm pressure under the feed ratio $CH_4:CO_2:N_2$ - 1:1:8, (36 mL/min).

constant throughout when the reaction is carried out in presence of feed, as shown in Fig. 14c. A similar mechanism was also observed in the DRIFT studies. In general, oxygen vacancies can be formed in the reducing environment (i.e., CH_4) and consumed in the oxidizing environment (i.e., CO_2), generating reactive oxygen species such as O_2^-, O_2^{2-}.

Room temperature Electron Paramagnetic Resonance (EPR) spectroscopy is widely used to identify the chemical species that have unpaired electrons or single electrons trapped at V_o sites [77]. Thus, the room-temperature EPR spectrum of $2NP/CeO_2$ catalyst was recorded, as shown in Fig. S6 (supporting information). The EPR spectrum of $2NP/CeO_2$ catalyst exhibited two strong, distinct axial signals with the g value of 2.004 and 2.001, assigned to the electrophilic superoxide oxygen (O_2^-) species trapped by V_o [14,57,68]. It has to be noted that these V_o sites can trap superoxide and peroxide, but peroxide (O_2^{2-}) species are EPR silent due to a lack of unpaired electrons [77].

3.5. Catalyst performance and evaluation

The activity of all the synthesized samples was tested for DRM at atmospheric pressure by varying reaction parameters and Ni loading. Fig. 15a-c exhibited temperature effect on CH_4 conversion, CO_2 conversion and H_2/CO ratio. The conversion of CO_2 and CH_4 increases gradually as the temperature increases, owing to the endothermic nature of DRM [78]. Catalysts synthesized by the solution combustion method activate CH_4 and CO_2 at 350 °C in the following order: $2NP/CeO_2$ > $4NP/CeO_2$ > $1NP/CeO_2$, while the impregnated catalyst ($2NP/CeO_2^{imp}$) was inactive at this temperature. This low-temperature activation of CH_4 and CO_2 is assisted by forming V_o sites (oxygen vacancies) and is consistent with the trend of A_{F2g}/A_D and O_V/O_V+O_L ratio. The low-temperature (350 °C) stability test over the solution combustion catalysts (Fig. 15d) revealed remarkable stability of $2NP/CeO_2$ catalysts, whereas the $1NP/CeO_2$ and $4NP/CeO_2$ catalyst showed a slight loss in their activity after 4 h of reaction. At low temperatures, CO_2 conversion was higher than the CH_4 conversion due to the RWGS [23,37]. According to thermodynamics, CO_2 activation is preferred at low temperatures, whereas CH_4 activation occurs at temperatures slightly higher than CO_2 activation temperatures [46]. RWGS reduce the H_2/CO ratio by utilizing H_2 to produce CO (Eq. 4). Solution combustion catalysts minimize the impact of RWGS (side reaction), yielding a higher H_2/CO ratio than $2NP/CeO_2^{imp}$ (Fig. 15c).

The effect of temperature at 600–700 °C was studied in detail to diminish the impact of RWGS and methane cracking to get the selectively dry reforming with H_2/CO ratio of 1. At 675 °C, the conversion of CO_2 and CH_4 becomes equal, yielding H_2/CO ratio equal to one (Fig. 15c). On further increase in temperature, an increase in CH_4 conversion over the CO_2 conversion and a higher H_2/CO ratio > 1 indicate methane cracking. So, 675 °C temperature has been selected as an optimum temperature for further analysis. At 675 °C, the reactivity order is in the following order: $2NP/CeO_2$ > $4NP/CeO_2$ > $1NP/CeO_2$ > $2NP/CeO_2^{imp}$ and the H_2/CO ratio is 1 for all the catalysts except $2NP/CeO_2^{imp}$ catalyst (0.94), suggesting that the RWGS reaction is still taking place over the $2NP/CeO_2^{imp}$ catalyst. The higher activity and selectivity of the combustion catalyst are attributed to the formation of oxygen vacancies
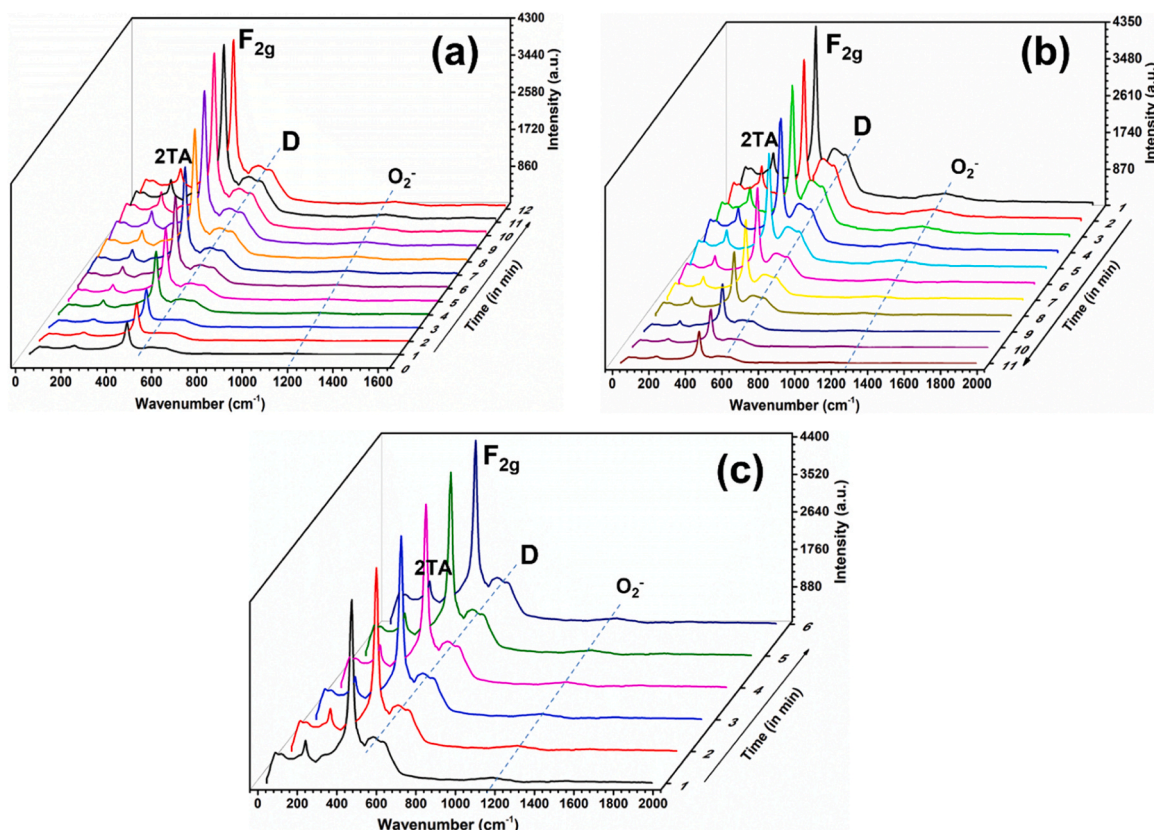
Fig. 14. *In-situ* Raman spectra in presence of CO_2 (a), CH_4 (b), and feed (c) ($CH_4:CO_2:N_2$ - 1:1:8) at 350 °C.
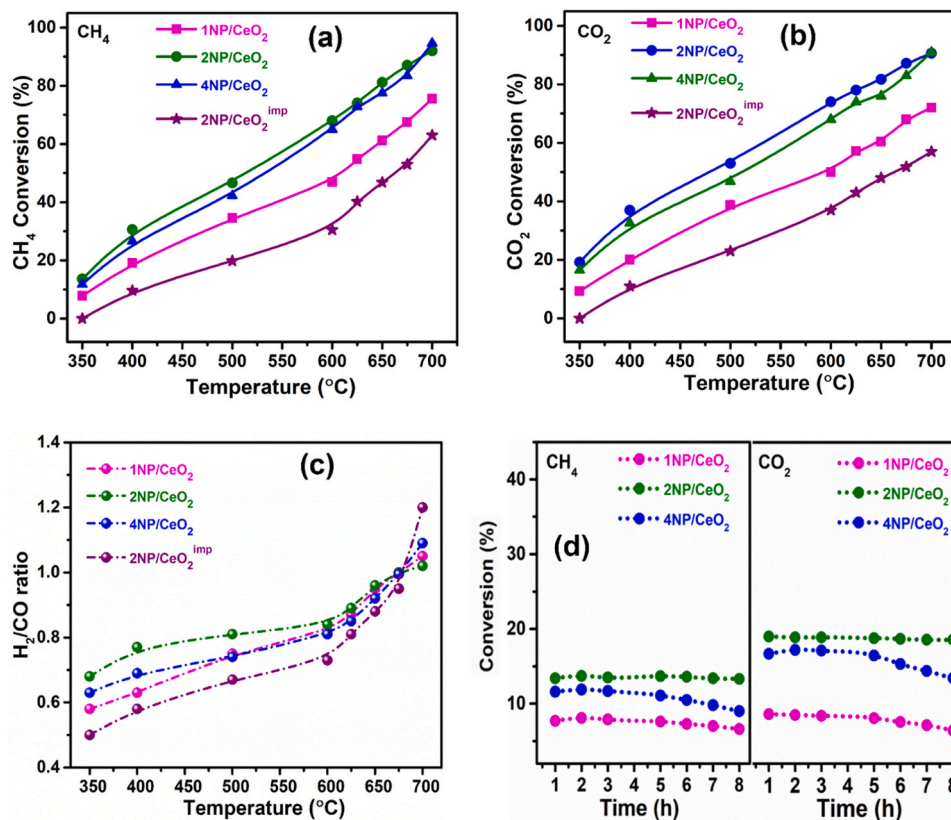

Fig. 15. Effect of temperature (300–700 °C) on CH_4 conversion (a), CO_2 conversion (b), H_2/CO ratio (c), and (d) 8 h stability test of $1NP/CeO_2$, $2NP/CeO_2$, and $4NP/CeO_2$ catalysts at 350 °C (Reaction condition: Pressure = 1 atm, Temperature = 300–700 °C (for 15a-c), GHSV = 60,000 mL.h^{-1}.g^{-1}, TOS = 8 h and Feed ratio = $CH_4:CO_2:N_2$ - 1:1:8).

by the incorporation of Ni and Pt metal ions into the ceria lattice and the formation of smaller metal nanoparticles (~2 nm). High metal dispersion provides more active sites for reactants, resulting in increased activity [78].

The stability test was performed at optimum conditions (GHSV-60,000 mL.h^{-1}.g^{-1}, temperature-675 °C). Fig. 16a shows the 30 h stability test (time-on-stream) of catalysts. In solution combustion catalysts, 4NP/CeO$_2$ catalysts showed a 7% decrease in initial activity, while 2NP/CeO$_2$ and 1NPCeO$_2$ were found to be stable without any loss in their activity. The loss in the activity of 4NP/CeO$_2$ can be due to the high loading of Ni by which Ni nanoparticles present on the surface get sintered. On the other hand, the 2NP/CeO$_2^{imp}$ catalyst shows a ~23% decrease in activity after 30 h of reaction due to the sintering and coke deposition over the catalyst surface (discussed later). The smaller nanoparticles provide a strong metal-support interaction, which resists the catalyst against sintering and coking [79]. Therefore, the catalysts prepared by the solution combustion method showed better stability than the impregnated catalyst. The 2NP/CeO$_2$ catalyst exhibited remarkable stability with higher conversion (~86%) of CO$_2$ and CH$_4$ and 100% syngas selectivity. Therefore, a more extended stability test (700 h) was carried out over the 2NP/CeO$_2$ catalyst (Fig. 16b). We did not observe any significant change in activity and selectivity of syngas (inset of Fig. 16b) throughout the reaction. The remarkable stability of 2NP/CeO$_2$ catalyst is attributed to higher oxygen vacancies (V$_o$), which are regeneratable during the DRM reaction. The oxygen species (O$_2^-$, O$_2^{2-}$) adsorbed on these V$_o$ sites are highly reactive, firstly consumed for the oxygen-assisted CH$_4$ activation and later regenerated by the dissociation of CO$_2$ into CO and O*. This cycle continues throughout the reaction.

In catalytic reactions, the diffusion of a reactant gas from the bulk fluid (i.e., carrier gas) to the catalyst surface (external diffusion) and diffusion from the catalyst surface to the catalyst pore (internal diffusion) could affect the rate of reaction. Similarly, temperature gradients could develop between the bulk fluid, catalyst surface and catalyst pores due to heat release (exothermic reaction) or absorption (endothermic reaction). To check whether external and internal diffusion and heat transfer limitations exist in 2NP/CeO$_2$, various criteria were evaluated (given in supporting information). The catalyst was found to be free from internal diffusion and heat transfer limitations.

3.6. Structure-activity correlation

In catalyst performance, presence of oxygen vacancies showed an important factor in defining catalytic activity and stability. Therefore, the amount of oxygen vacancies (O$_V$/O$_V$+O$_L$) was plotted against CH$_4$ and CO$_2$ conversion in order to get the structure-activity correlation. As illustrated by Fig. 17a, a linear relationship exists between CH$_4$/CO$_2$ conversion and O$_V$/O$_V$+O$_L$ ratio. The catalyst with the highest O$_V$/O$_V$+O$_L$ ratio exhibited the highest conversion of CH$_4$/CO$_2$. Furthermore, a linear correlation between O$_V$/O$_V$+O$_L$ ratio against A$_{F2g}$/A$_D$ ratio (Fig. 17b) and O$_V$/O$_V$+O$_L$ ratio against O$_{II}$ species (reactive oxygen species estimated by O$_2$-TPD (Fig. 17c), indicating that the catalyst which has a higher extent of defects have the higher amount of reactive oxygen species (O$_2^-$, O$_2^{2-}$), simultaneously have the higher amount of O$_V$/O$_V$+O$_L$ ratio. Hence, we can conclude that the oxygen vacancies are the key factor which affects the catalytic activity. The 2NP/CeO$_2$ catalyst has the highest amount of A$_{F2g}$/A$_D$, O$_{II}$ species, and O$_V$/O$_V$+O$_L$ ratio and shows the highest catalytic activity.

3.7. Temperature-programmed surface reaction

Furthermore, to elucidate the role of reactive oxygen species in methane activation, a CH$_4$ temperature-programmed surface reaction (CH$_4$-TPSR) experiment was carried out over 2NP/CeO$_2$. For comparison purposes, the TPSR experiment was also carried out over 2NP/CeO$_2^{imp}$ catalyst. The CH$_4$-TPSR test was performed in the flow of 10% CH$_4$/He at 30 mL/min from 50° to 850°C and MS signal of H$_2$ ($m/z = 2$), H$_2$O ($m/z = 18$), CO ($m/z = 28$), and CO$_2$ ($m/z = 44$) were continuously monitored during the experiment. A detailed description is given in the supporting information. 2NP/CeO$_2$ catalyst shows the significant formation of CO and H$_2$ starting at ~300 °C, as shown in Fig. 18a. On the other hand, 2NP/CeO$_2^{imp}$ catalyst primarily contributes to the formation of CO$_2$ and H$_2$O rather than CO and H$_2$ (Fig. 18b). The formation of CO and H$_2$ over the 2NP/CeO$_2$ catalyst in the absence of CO$_2$ firmly demonstrated that the surface-active oxygen species are the active and selective oxygen sites for the activation of CH$_4$ and the production of syngas selectively during DRM.
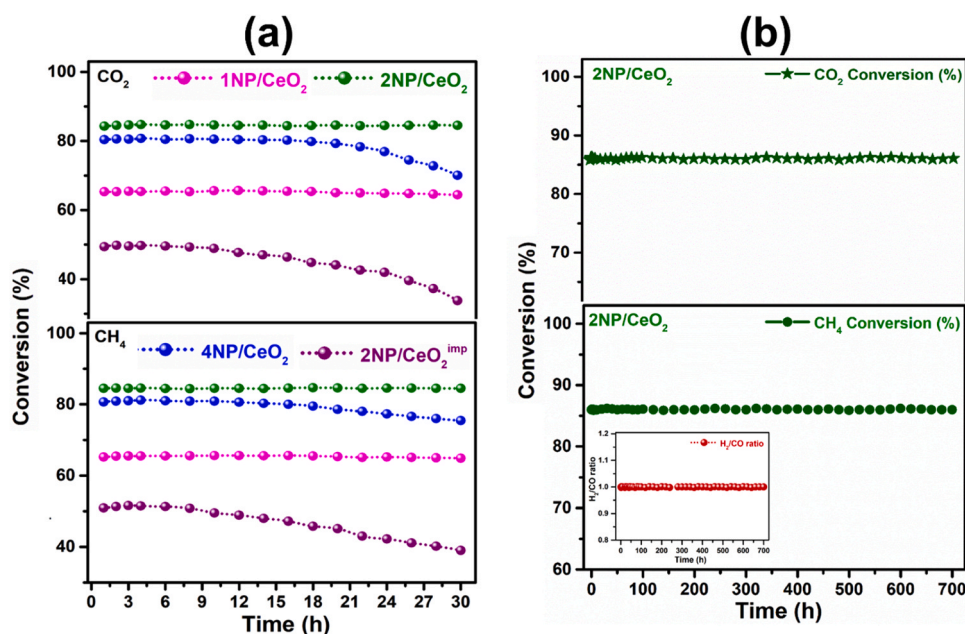

Fig. 16. Time-on-stream study, (a) 30 h stability test over the combustion catalyst, and (b) 700 h stability test over the 2NP/CeO$_2$ catalyst (Reaction condition: Temperature = 675 °C, Pressure = 1 atm, GHSV = 60,000 mL.h^{-1}.g^{-1}, Feed ratio = CH$_4$:CO$_2$:N$_2$ - 1:1:8).
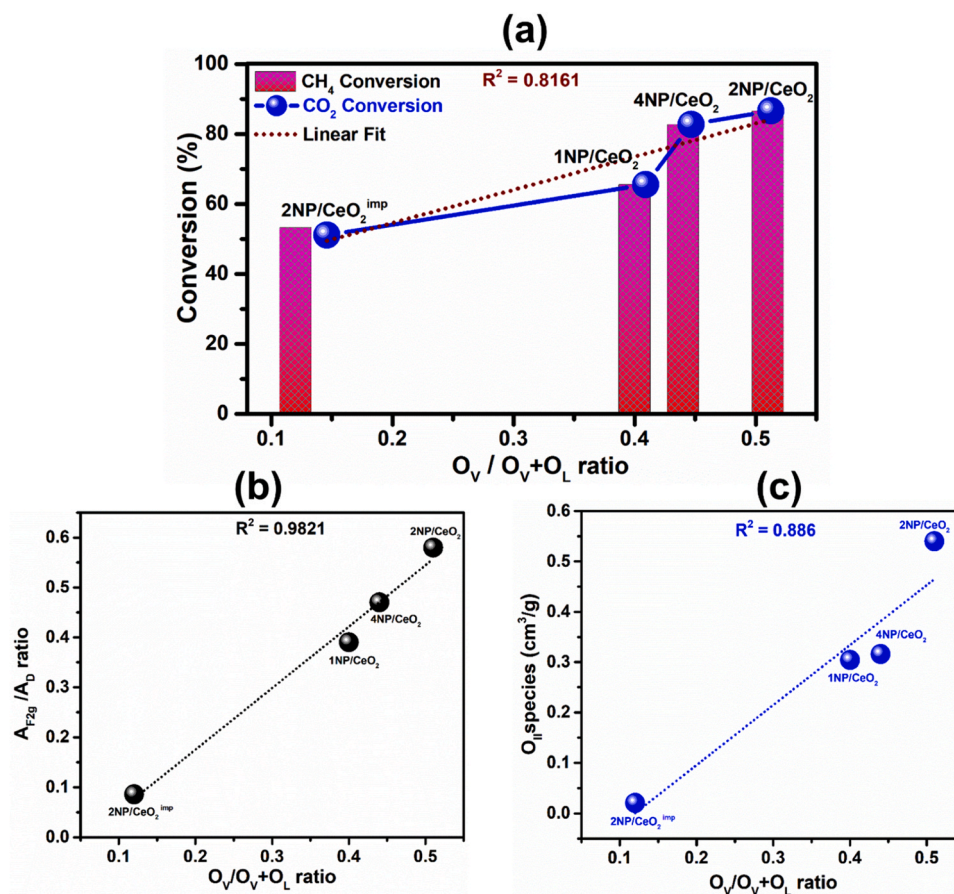
Fig. 17. Structure-activity relationship, (a) O_V/O_V+O_L ratio V/s Conversion of CH_4/CO_2, (b) A_{F2g}/A_D ratio V/s O_V/O_V+O_L ratio, and (c) O_{II} species V/s O_V/O_V+O_L ratio.
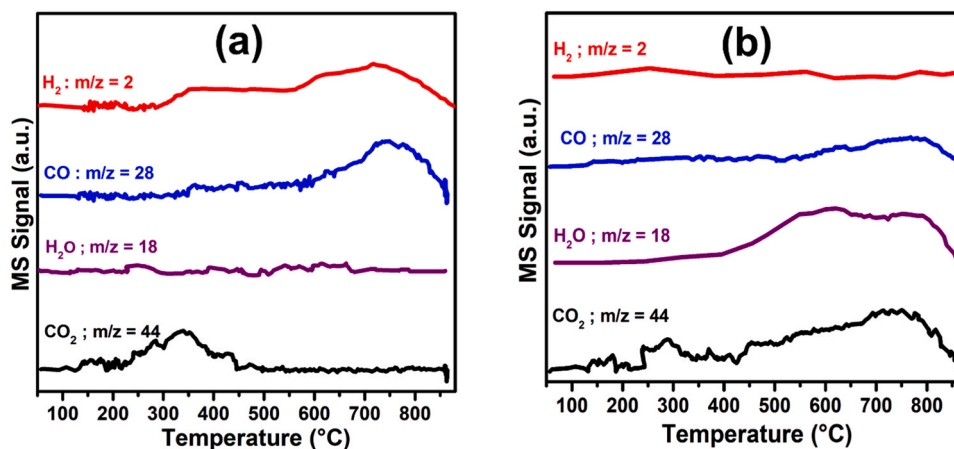
Fig. 18. CH_4-TPSR over the (a) $2NP/CeO_2$ and (b) $2NP/CeO_2^{imp}$ catalysts.

3.8. Theoretical study

From the experimental results, we have found that the DRM reaction over the NiPt-CeO$_2$ catalyst proceeds through the formation of CH_xO intermediate. Therefore, DFT computations were performed to study the DRM reaction mechanism, as given in SI (S1.3), over the NiPt-doped CeO$_2$ (111) surface shown as the free energy profile diagram in Fig. 19, whereas the DFT optimized geometry of surface adsorbed species has been shown in Fig. 20.

The DRM reaction over the NiPt-doped CeO$_2$ (111) surface was initiated through the activation of CO_2 molecule at the oxygen vacancy site (V_o) of NiPt-CeO$_2$ (111) surface active center. The CO_2 molecule was adsorbed at the NiPt-CeO$_2$ (111) surface active center, forming Pt-C bond (2.1 Å) as shown in Fig. 20(a), where one of the O atoms of CO_2 points towards the oxygen vacancy site. The free energy of CO_2 adsorption was found to be endergonic by 41.2 kcal/mol due to the loss of gas-phase entropy of the CO_2 molecule. The C-O bond of CO_2 molecule was finally broken (Fig. 19(a) → (b)), forming adsorbed CO molecule and the O atom was transferred to the V_o site to fill the oxygen vacancy, as shown in Fig. 20(b). The CO_2 activation barrier was
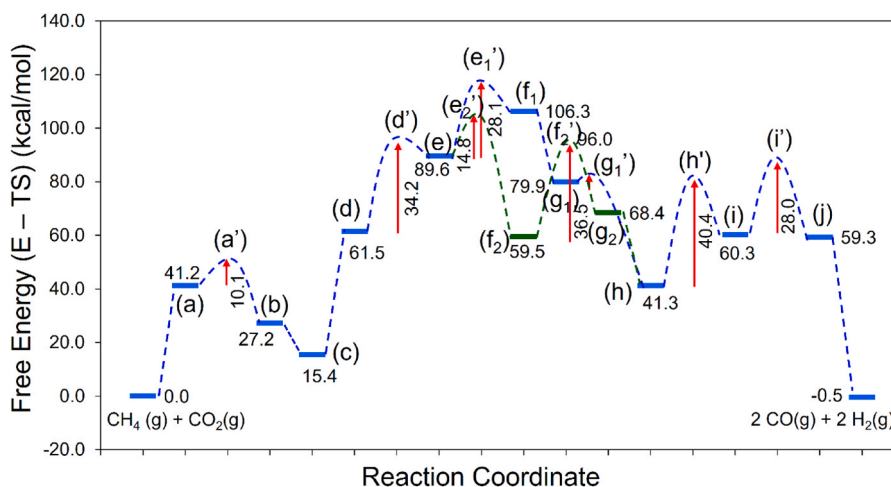
Fig. 19. Free energy profile of dry reforming of methane over the NiPt-CeO$_2$ (111) surface at 912 K. Reaction and activation energies are in kcal/mol.

calculated to be 10.1 kcal/mol, whereas the reaction free energy was exergonic by −14.0 kcal/mol (Fig. 19), indicating high activity of NiPt-doped CeO$_2$ (111) surface for the CO$_2$ activation. The CO molecule adsorbed at the Pt metal site was subsequently desorbed with an exergonic desorption energy of −11.8 kcal/mol (Fig. 19(b) → (c)). The reaction then proceeds with the adsorption of the CH$_4$ molecule having an endergonic energy of 46.1 kcal/mol, as shown in Fig. 19(c) → (d). The adsorption geometry of CH$_4$ at NiPt-CeO$_2$ (111) active site has been displayed in Fig. 20(d). Firstly, C-H bond of adsorbed CH$_4$ molecule activates at the Pt center, forming dissociated CH$_3$ and H, as shown in Fig. 20(e), where both CH$_3$ and H species were bonded to the Pt atom. The activation barrier for methane C-H bond dissociation (Fig. 19(d) → (e)) was calculated to be 34.2 kcal/mol, whereas the reaction free energy was calculated to be endergonic by 28.1 kcal/mol. Two pathways were explored after this point, where in the first pathway (Fig. 19, blue color), the adsorbed CH$_3$ was further dehydrogenated to CH$_2$ at the Pt metal site, and then the CH$_2$ migrated to the oxygen adsorbed at the vacancy site to form CH$_2$O, whereas in the second pathway (Fig. 19, green color) the CH$_3$ migrate to the oxygen vacancy site to form CH$_3$O. The dehydrogenation of adsorbed CH$_3$ + H to CH$_2$ + H$_2$ has been displayed in Fig. 19(e) → (f$_1$). The activation barrier and reaction free energies for this second dehydrogenation step were calculated to be 28.1 kcal/mol (Fig. 19(e) → (e')) and 16.7 kcal/mol (Fig. 19(e) → (f$_1$)), respectively. The desorption of H$_2$ molecule was calculated to be exergonic by −26.4 kcal/mol (Fig. 19(f$_1$) → (g$_1$)). In the subsequent reaction step, the adsorbed CH$_2$ readily migrates with a small activation barrier of 2.2 kcal/mol (Fig. 19(g$_1$) → (g$_1$')) to the O atom sitting at the oxygen vacancy site forming OCH$_2$ species, as shown in Fig. 20(h). The formation of OCH$_2$ species was found to be highly favorable with exergonic reaction free energy of −38.7 kcal/mol (Fig. 19(g$_1$) → (h)). Similarly, in the second pathway, as shown in Fig. 19 (green color), the adsorbed CH$_3$ first migrate to the oxygen atom sitting at the oxygen vacancy site forming OCH$_3$ species Fig. 20(f$_2$). The formation of OCH$_3$ species (Fig. 19(e) → (f$_2$)) was also found to be highly favorable with the exergonic free energy of −30.1 kcal/mol and a small activation barrier of 14.8 kcal/mol. Next, the OCH$_3$ species undergo dehydrogenation to form the OCH$_2$ species, whereas the two H atoms also combine to form H$_2$ molecule, as has been shown in Fig. 20(g$_2$). The activation barrier and reaction free energy for the OCH$_3$ dehydrogenation was calculated to be 36.5 kcal/mol and 8.9 kcal/mol, respectively (Fig. 19). The H$_2$ molecule was subsequently desorbed from the surface with desorption free energy of −27.1 kcal/mol (Fig. 19(g$_2$) → (h)). The adsorbed OCH$_2$ at the NiPt-CeO$_2$ (111) surface (Fig. 20(h)) then undergoes further dehydrogenation (Fig. 19(h) → (i)) to form HCO and H (Fig. 20(i)), with activation barrier of 40.4 kcal/mol and reaction free energy 19.0 kcal/

mol, indicating high stabilization of the OCH$_2$ species during the DRM reaction over the NiPt-CeO$_2$ (111) surface. Next, the adsorbed HCO species undergo dehydrogenation to form CO (Fig. 19(i) → (j)), whereas two H atoms form H$_2$ molecule, as has been shown in Fig. 20(j). The activation barrier for HCO dehydrogenation was measured to be 28.0 kcal/mol, whereas the reaction free energy was calculated to be −1.0 kcal/mol (Fig. 19). The oxygen vacancy site was also regenerated in this step, as shown in Fig. 20(j). Finally, the surface adsorbed CO and H$_2$ molecules desorbed from the surface, regenerating the NiPt-CeO$_2$ (111) surface active center for the next catalytic cycle.

3.9. Coke analysis of spent catalyst

Coke study of all samples was performed after a 30 h stability test to know the amount and types of carbonaceous species deposited over the catalyst surface. Figs. 21a and 21b show the Raman spectra and TGA patterns of spent catalysts, respectively. The amount of carbon deposited over the 2NP/CeO$_2$ and 1NP/CeO$_2$ catalysts estimated by TGA was found to be 0.35% and 0.7%, respectively (Fig. 21(b)), which may be due to the removal of moisture. On the other hand, 4NP/CeO$_2$ shows 3.3%, and 2NP/CeO$_2^{imp}$ catalyst shows the highest amount of coke deposition by 16.8% weight loss, which is associated with soft and hard coke [19,47]. The obtained results are well supported by the Raman analysis.

In Raman spectra, D and G bands at about 1341 and 1574 cm^{-1} are linked to the amorphous (disordered and soft) and graphitic (ordered and hard) coke [29,59,80]. The absence of D and G bands in 2NP/CeO$_2$ and 1NP/CeO$_2$ catalysts shows a coke resistance nature. Nevertheless, 4NP/CeO$_2$ and 2NP/CeO$_2^{imp}$ catalysts exhibited both the D and G bands, but the higher ratio of I$_G$/I$_D$ bands over the 2NP/CeO$_2^{imp}$ (2.17) compared to 4NP/CeO$_2$ (0.87), indicating that the 2NP/CeO$_2^{imp}$ catalyst has the higher degree of graphitic carbon. The formation of graphitic coke can also be seen in the TEM images (Fig. S8(d)) and XRD pattern of spent 2NP/CeO$_2^{imp}$ (Fig. S1). Conversely, the TEM images of 2NP/CeO$_2$ and 1NP/CeO$_2$ catalysts do not show any significant coke deposition and structural changes (Fig. S8a and b). The smaller nanoparticles provide better coke-resistivity during the reaction. Earlier studies showed that Ni nanoparticles smaller than 7 nm can effectively suppress sintering and coking. [79,81]. The XRD, TGA and Raman analysis of spent 2NP/CeO$_2$ were also performed after a 700 h time-on-stream stability test, shown in Fig. S9(a-c), respectively. The XRD pattern of the spent 2NP/CeO$_2$ catalyst shows an increment in the intensities of ceria peaks after 700 h time-on-stream reaction, indicating an increment in the crystallite size of the spent catalyst. The TGA (Fig. S9b) and Raman (Fig. S9c) analysis of the spent 2NP/CeO$_2$ catalyst showed the excellent coke resistance
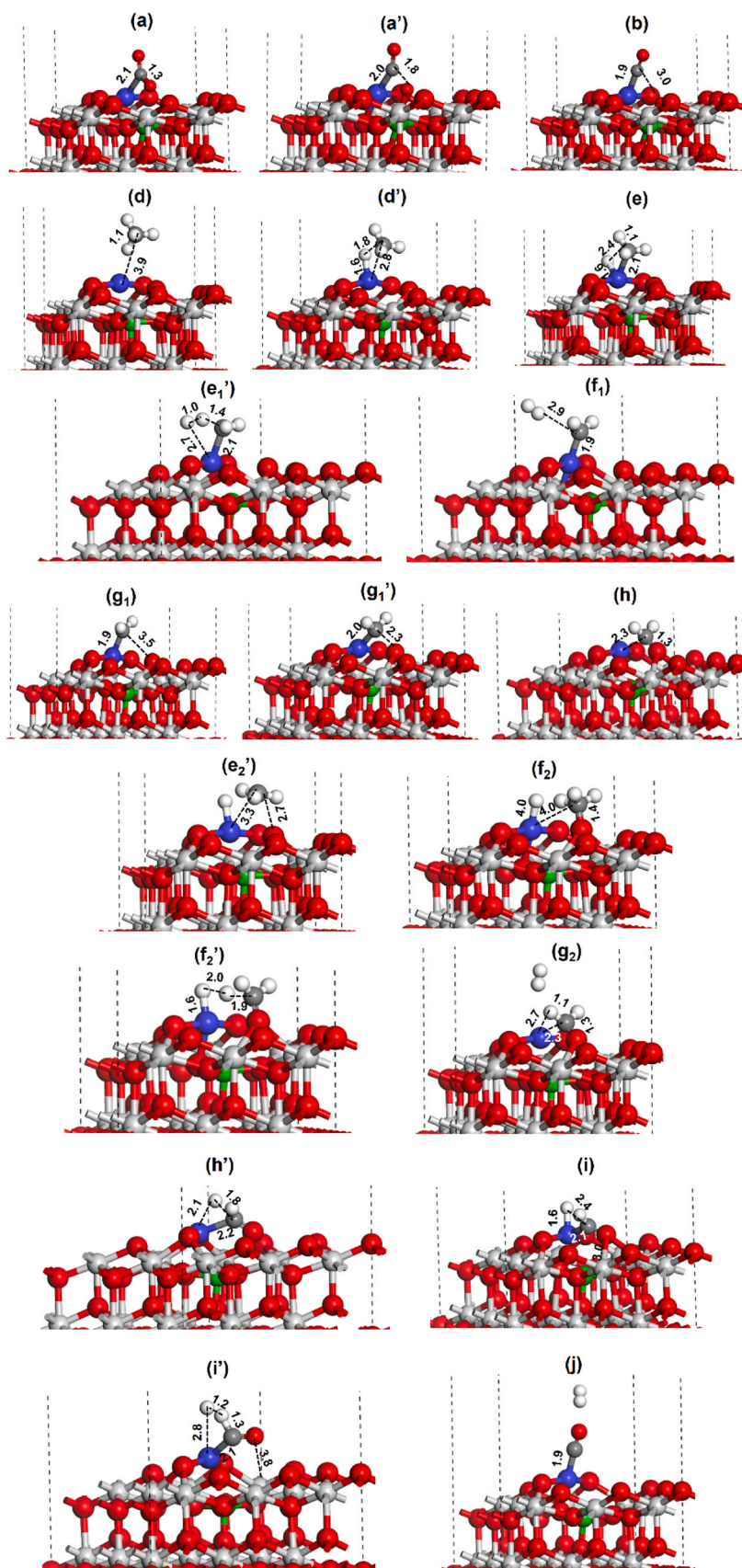
Fig. 20. DFT optimized geometry of surface adsorbed species formed during the DRM reaction over the NiPt-CeO$_2$ (111) surface. Color code: Ce (silver), Ni (green), Pt (blue), (O red), and C (grey). Reaction and activation energies are in kcal/mol.
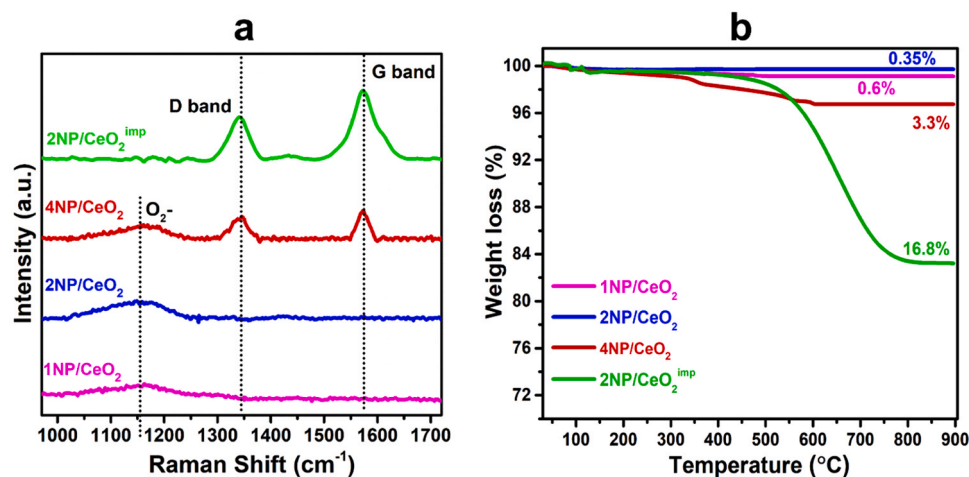
Fig. 21. Raman spectra (a) and TGA graphs (b) of spent $1NP/CeO_2$, $2NP/CeO_2$, $4NP/CeO_2$, $2NP/CeO_2^{imp}$ catalysts after 30 h TOS stability test (Reaction condition-temp. 675 °C, TOS 30 h).

nature of $2NP/CeO_2$ catalysts.

4. Conclusion

The bimetallic Ni-Pt/CeO₂ defect-rich catalysts were prepared by solution-combustion method by varying the Ni loading (1–4 wt%) and tested for DRM reaction. Lattice parameter calculation by XRD analysis revealed that the catalyst with 2 wt% of Ni ($2NP/CeO_2$) exhibited a higher extent of solid solution formation. The extent of generation of defected sites/oxygen vacancies (V_o) are proportional to the extent of solid-solution formation and follows the following order: $2NP/CeO_2$ > $4NP/CeO_2$ > $1NP/CeO_2$ >> $2NP/CeO_2^{imp}$ and linearly correlated with the amount of reactive oxygen species (O_{II}) estimated from O_2-TPD analysis. $2NP/CeO_2$ catalyst exhibited superior activity by showing ~86% conversion of CH_4/CO_2 and 100% selectivity of syngas with H_2/CO ratio of 1 at 675 °C. During the stability test of 700 h TOS, the catalyst maintains remarkable stability without any loss in conversion or selectivity. CH_4-TPSR revealed that the surface reactive oxygen species are more selective toward the formation of syngas. Reactive oxygen species (O_2^-, O_2^{2-}) trapped on defective sites can activate the CH_4/CO_2 at low temperature (350 °C). The activation of CH_4 takes place by forming a CH_xO intermediate with the assistance of surface reactive oxygen species. DFT calculation also suggested the facile formation of CH_2O and CH_3O species during the DRM reaction over the NiPt-CeO₂ (111) surface having a small activation barrier and high exergonic reaction free energy. The consumption of surface reactive oxygen species generates the oxygen vacancies (V_o sites), where CO_2 gets activated and dissociates into CO and O* to revive the surface reactive oxygen species.

CRediT authorship contribution statement

Rubina Khatun: designed the experiment and involved catalyst synthesis, reaction study and optimization, data analysis, data compilation, and drafting of the manuscript. Rohan Singh Pal: catalyst synthesis and characterization-RAMAN. Mohammad Ahmad Shoeb: reaction optimization. Deepak Kurana: DFT calculation. Shubham Singhl: catalysts synthesis. Nazia Siddiqui: catalysts characterization (TPDs). Mukesh Kumar Poddar: catalyst characterization (TPR). Tuhin Suvra Khan: DFT calculation. Rajaram Bal: supervised the study and was responsible for the overall direction of the study and the final drafting of the manuscript.

Declaration of Competing Interest

All the authors declare that they have no known competing financial

interests or personal relationships that could have appeared to influence the work reported in this paper.

Data Availability

The authors do not have permission to share data.

Appendix A. Supporting information

Supplementary data associated with this article can be found in the online version at doi:10.1016/j.apcatb.2023.123243.

References

[1] V. UNFCCC, Adoption of the Paris agreement, Propos. Pres. 282 (2015).
[2] J. Rogelj, M. Den Elzen, N. Höhne, T. Fransen, H. Fekete, H. Winkler, R. Schaeffer, F. Sha, K. Riahi, M. Meinshausen, Paris Agreement climate proposals need a boost to keep warming well below 2 C, Nature 534 (2016) 631–639.
[3] R. Zhou, M. Mohamedali, Y. Ren, Q. Lu, N. Mahinpey, Facile synthesis of multi-layered nanostructured Ni/CeO2 catalyst plus in-situ pre-treatment for efficient dry reforming of methane, Appl. Catal. B: Environ. 316 (2022), 121696.
[4] M. Li, A.C. van Veen, Tuning the catalytic performance of Ni-catalysed dry reforming of methane and carbon deposition via Ni-CeO2-x interaction, Appl. Catal. B: Environ. 237 (2018) 641–648.
[5] T.G. de Araújo Moreira, J.F.S. de Carvalho Filho, Y. Carvalho, J.M.A.R. de Almeida, P.N. Romano, E.F. Sousa-Aguiar, Highly stable low noble metal content rhodium-based catalyst for the dry reforming of methane, Fuel 287 (2021), 119536.
[6] M. García-Diéguez, I. Pieta, M. Herrera, M. Larrubia, L. Alemany, Improved Pt-Ni nanocatalysts for dry reforming of methane, Appl. Catal. A: Gen. 377 (2010) 191–199.
[7] J. Niu, F. Guo, J. Ran, W. Qi, Z. Yang, Methane dry (CO₂) reforming to syngas (H2/CO) in catalytic process: from experimental study and DFT calculations, Int. J. Hydrog. Energy 45 (2020) 30267–30287.
[8] M.A.A. Aziz, H.D. Setiabudi, L.P. Teh, M. Asmadi, J. Matmin, S. Wongsakulphasatch, High-performance bimetallic catalysts for low-temperature carbon dioxide reforming of methane, Chem. Eng. Technol. 43 (2020) 661–671.
[9] M. Shah, P. Mondal, A.K. Nayak, A. Bordoloi, Advanced titania composites for efficient CO₂ reforming with methane: statistical method vs. experiment, J. CO₂ Util. 39 (2020), 101160.
[10] G. Zhang, J. Liu, Y. Xu, Y. Sun, A review of CH4CO2 reforming to synthesis gas over Ni-based catalysts in recent years (2010–2017), Int. J. Hydrog. Energy 43 (2018) 15030–15054.

[11] Y. Xu, X. Du, L. Shi, T. Chen, H. Wan, P. Wang, S. Wei, B. Yao, J. Zhu, M. Song, Improved performance of Ni/Al2O3 catalyst deriving from the hydrotalcite precursor synthesized on Al2O3 support for dry reforming of methane, Int. J. Hydrog. Energy 46 (2021) 14301–14310.

[12] D.G. Araiza, D.G. Arcos, A. Gómez-Cortés, G. Díaz, Dry reforming of methane over Pt-Ni/CeO2 catalysts: effect of the metal composition on the stability, Catal. Today 360 (2021) 46–54.

[13] E. Lovell, Y. Jiang, J. Scott, F. Wang, Y. Suhardja, M. Chen, J. Huang, R. Amal, CO2 reforming of methane over MCM-41-supported nickel catalysts: altering support acidity by one-pot synthesis at room temperature, Appl. Catal. A: Gen. 473 (2014) 51–58.

[14] Y. Zhang, Y. Zu, D. He, J. Liang, L. Zhu, Y. Mei, Y. Luo, The tailored role of "defect" sites on γ-alumina: a key to yield an efficient methane dry reforming catalyst with superior nickel utilization, Appl. Catal. B: Environ. (2022), 121539.

[15] S. Das, M. Shah, R.K. Gupta, A. Bordoloi, Enhanced dry methane reforming over Ru decorated mesoporous silica and its kinetic study, J. CO2 Util. 29 (2019) 240–253.

[16] S. Li, J. Gong, Strategies for improving the performance and stability of Ni-based catalysts for reforming reactions, Chem. Soc. Rev. 43 (2014) 7245–7256.

[17] J. Niu, Y. Wang, S.E. Liland, S.K. Regli, J. Yang, K.R. Rout, J. Luo, M. Rønning, J. Ran, D. Chen, Unraveling enhanced activity, selectivity, and coke resistance of Pt–Ni bimetallic clusters in dry reforming, ACS Catal. 11 (2021) 2398–2411.

[18] V. Palma, F. Castaldo, P. Ciambelli, G. Iaquaniello, CeO2-supported Pt/Ni catalyst for the renewable and clean H2 production via ethanol steam reforming, Appl. Catal. B: Environ. 145 (2014) 73–84.

[19] R. Khatun, S. Bhandari, M.K. Poddar, C. Samanta, T.S. Khan, D. Khurana, R. Bal, Partial oxidation of methane over high coke-resistant bimetallic Pt-Ni/CeO2 catalyst: profound influence of Pt addition on stability, Int. J. Hydrog. Energy 47 (2022) 38895–38909.

[20] Y.H. Hu, Advances in catalysts for CO2 reforming of methane, ACS Symp. . Ser. 1056 (2010) 155–174.

[21] W. Yu, M.D. Porosoff, J.G. Chen, Review of Pt-based bimetallic catalysis: from model surfaces to supported catalysts, Chem. Rev. 112 (2012) 5780–5817.

[22] P. Corbo, F. Migliardini, Hydrogen production by catalytic partial oxidation of methane and propane on Ni and Pt catalysts, Int. J. Hydrog. Energy 32 (2007) 55–66.

[23] D. Shen, Z. Li, J. Shan, G. Yu, X. Wang, Y. Zhang, C. Liu, S. Lyu, J. Li, L. Li, Synergistic Pt-CeO2 interface boosting low temperature dry reforming of methane, Appl. Catal. B: Environ. 318 (2022), 121809.

[24] S. Das, A. Jangam, S. Jayaprakash, S. Xi, K. Hidajat, K. Tomishige, S. Kawi, Role of lattice oxygen in methane activation on Ni-phyllosilicate@ Ce1-xZrxO2 core-shell catalyst for methane dry reforming: Zr doping effect, mechanism, and kinetic study, Appl. Catal. B: Environ. 290 (2021), 119998.

[25] V.M. Gonzalez-Delacruz, F. Ternero, R. Pereñíguez, A. Caballero, J.P. Holgado, Study of nanostructured Ni/CeO2 catalysts prepared by combustion synthesis in dry reforming of methane, Appl. Catal. A: Gen. 384 (2010) 1–9.

[26] R.O. da Fonseca, A.R. Ponseggi, R.C. Rabelo-Neto, R.C. Simões, L.V. Mattos, F. B. Noronha, Controlling carbon formation over Ni/CeO2 catalyst for dry reforming of CH4 by tuning Ni crystallite size and oxygen vacancies of the support, J. CO2 Util. 57 (2022), 101880.

[27] I. Luisetto, S. Tuti, C. Romano, M. Boaro, E. Di Bartolomeo, J.K. Kesavan, S. S. Kumar, K. Selvakumar, Dry reforming of methane over Ni supported on doped CeO2: new insight on the role of dopants for CO2 activation, J. CO2 Util. 30 (2019) 63–78.

[28] X. Du, D. Zhang, L. Shi, R. Gao, J. Zhang, Morphology dependence of catalytic properties of Ni/CeO2 nanostructures for carbon dioxide reforming of methane, J. Phys. Chem. C 116 (2012) 10009–10016.

[29] D. Guo, Y. Lu, Y. Ruan, Y. Zhao, Y. Zhao, S. Wang, X. Ma, Effects of extrinsic defects originating from the interfacial reaction of CeO2-x-nickel silicate on catalytic performance in methane dry reforming, Appl. Catal. B: Environ. 277 (2020), 119278.

[30] W. Shan, Z. Feng, Z. Li, J. Zhang, W. Shen, C. Li, Oxidative steam reforming of methanol on Ce0. 9Cu0. 1OY catalysts prepared by deposition–precipitation, coprecipitation, and complexation–combustion methods, J. Catal. 228 (2004) 206–217.

[31] T. Sagar, D. Padmakar, N. Lingaiah, P. Sai, Prasad, Influence of solid solution formation on the activity of CeO2 supported Ni–Cu mixed oxide catalysts in dry reforming of methane, Catal. Lett. 149 (2019) 2597–2606.

[32] W. Kang, A. Varma, Hydrogen generation from hydrous hydrazine over Ni/CeO2 catalysts prepared by solution combustion synthesis, Appl. Catal. B: Environ. 220 (2018) 409–416.

[33] S. Mahammadunnisa, P.M.K. Reddy, N. Lingaiah, C. Subrahmanyam, NiO/Ce 1− x Ni x O 2− δ as an alternative to noble metal catalysts for CO oxidation, Catal. Sci. Technol. 3 (2013) 730–736.

[34] B.M. Al–Swai, N.B. Osman, A. Ramli, B. Abdullah, A.S. Farooqi, B.V. Ayodele, D. O. Patrick, Low-temperature catalytic conversion of greenhouse gases (CO2 and CH4) to syngas over ceria-magnesia mixed oxide supported nickel catalysts, Int. J. Hydrog. Energy 46 (2021) 24768–24780.

[35] Y. Wang, L. Yao, S. Wang, D. Mao, C. Hu, Low-temperature catalytic CO2 dry reforming of methane on Ni-based catalysts: A review, Fuel Process. Technol. 169 (2018) 199–206.

[36] J. Yang, D. Gong, X. Lu, C. Han, H. Liu, L. Wang, Ni-CeO2/SBA-15 catalyst prepared by glycine-assisted impregnation method for low-temperature dry reforming of methane, Cryst 12 (2022) 713.

[37] R.K. Singha, S. Ghosh, S.S. Acharyya, A. Yadav, A. Shukla, T. Sasaki, A.M. Venezia, C. Pendem, R. Bal, Partial oxidation of methane to synthesis gas over Pt

[38] nanoparticles supported on nanocrystalline CeO 2 catalyst, Catal. Sci. Technol. 6 (2016) 4601–4615.

[38] L. Shi, W. Shen, G. Yang, X. Fan, Y. Jin, C. Zeng, K. Matsuda, N. Tsubaki, Formic acid directly assisted solid-state synthesis of metallic catalysts without further reduction: as-prepared Cu/ZnO catalysts for low-temperature methanol synthesis, J. Catal. 302 (2013) 83–90.

[39] F. Zhang, Z. Liu, X. Chen, N. Rui, L.E. Betancourt, L. Lin, W. Xu, Effects of Zr doping into ceria for the dry reforming of methane over Ni/CeZrO2 catalysts: in situ studies with XRD, XAFS, and AP-XPS, ACS Catal. 10 (2020) 3274–3284.

[40] A. Singhania, S.M. Gupta, Nickel nanocatalyst ex-solution from ceria-nickel oxide solid solution for low temperature CO oxidation, J. Nanosci. Nanotechnol. 18 (2018) 4614–4620.

[41] H. Sasaki, H. Matsushita, K. Sakamoto, T. Sakamoto, M. Maeda, Formation of Pt3O4 particles on PtO2–CeO2 solid solution, J. Phys. Chem. Solids 135 (2019), 109097.

[42] H.-H. Liu, Y. Wang, A.-P. Jia, S.-Y. Wang, M.-F. Luo, J.-Q. Lu, Oxygen vacancy promoted CO oxidation over Pt/CeO2 catalysts: A reaction at Pt–CeO2 interface, Appl. Surf. Sci. 314 (2014) 725–734.

[43] A. Miri, M. Sarani, M. Khatami, Nickel-doped cerium oxide nanoparticles: biosynthesis, cytotoxicity and UV protection studies, RSC Adv. 10 (2020) 3967–3977.

[44] F. Abbas, T. Jan, J. Iqbal, I. Ahmad, M.S.H. Naqvi, M. Malik, Facile synthesis of ferromagnetic Ni doped CeO2 nanoparticles with enhanced anticancer activity, Appl. Surf. Sci. 357 (2015) 931–936.

[45] Q. Dongsheng, L. Guanzhong, G. Yun, W. Yanqin, G. Yanglong, Effect of water vapor on the CO and CH4 catalytic oxidation over CeO2-MOx (M= Cu, Mn, Fe, Co, and Ni) mixed oxide, J. Rare Earths 28 (2010) 742–746.

[46] M. Shah, A. Bordoloi, A.K. Nayak, P. Mondal, Effect of Ti/Al ratio on the performance of Ni/TiO2-Al2O3 catalyst for methane reforming with CO2, Fuel Process. Technol. 192 (2019) 21–35.

[47] R.K. Singha, A. Shukla, A. Yadav, S. Adak, Z. Iqbal, N. Siddiqui, R. Bal, Energy efficient methane tri-reforming for synthesis gas production over highly coke resistant nanocrystalline Ni–ZrO2 catalyst, Appl. Energy 178 (2016) 110–125.

[48] R. Hamidi, R. Khoshbin, R. Karimzadeh, Facile fabrication, characterization and catalytic activity of a NiMo/Al 2 O 3 nanocatalyst via a solution combustion method used in a low temperature hydrodesulfurization process: the effect of fuel to oxidant ratio, RSC Adv. 10 (2020) 12439–12450.

[49] R.K. Singha, A. Shukla, A. Yadav, L.S. Konathala, R. Bal, Effect of metal-support interaction on activity and stability of Ni-CeO2 catalyst for partial oxidation of methane, Appl. Catal. B: Environ. 202 (2017) 473–488.

[50] Y. Li, B. Zhang, X. Tang, Y. Xu, W. Shen, Hydrogen production from methane decomposition over Ni/CeO2 catalysts, Catal. Commun. 7 (2006) 380–386.

[51] Q. Zhang, X. Liao, S. Liu, H. Wang, Y. Zhang, Y. Zhao, Tuning particle sizes and active sites of Ni/CeO2 catalysts and their influence on maleic anhydride hydrogenation, Nanomaterials 12 (2022) 2156.

[52] W. Shan, M. Luo, P. Ying, W. Shen, C. Li, Reduction property and catalytic activity of Ce1− XNiXO2 mixed oxide catalysts for CH4 oxidation, Appl. Catal. A: Gen. 246 (2003) 1–9.

[53] A. Jan, J. Shin, J. Ahn, S. Yang, K.J. Yoon, J.-W. Son, H. Kim, J.-H. Lee, H.-I. Ji, Promotion of Pt/CeO 2 catalyst by hydrogen treatment for low-temperature CO oxidation, RSC Adv. 9 (2019) 27002–27012.

[54] W. Shan, M. Fleys, F. Lapicque, D. Swierczynski, A. Kiennemann, Y. Simon, P.-M. Marquaire, Syngas production from partial oxidation of methane over Ce1− XNiXOY catalysts prepared by complexation–combustion method, Appl. Catal. A: Gen. 311 (2006) 24–33.

[55] R.-P. Ye, Q. Li, W. Gong, T. Wang, J.J. Razink, L. Lin, Y.-Y. Qin, Z. Zhou, H. Adidharma, J. Tang, High-performance of nanostructured Ni/CeO2 catalyst on CO2 methanation, Appl. Catal. B: Environ. 268 (2020), 118474.

[56] X. Zhou, J. Ling, W. Sun, Z. Shen, Fabrication of homogeneously Cu 2+/La 3+-doped CeO 2 nanosheets and their application in CO oxidation, J. Mater. Chem. A 5 (2017) 9717–9722.

[57] R.S. Pal, S. Rana, S.K. Sharma, R. Khatun, D. Khurana, T.S. Khan, M.K. Poddar, R. Sharma, R. Bal, Enhancement of oxygen vacancy sites of La2-xMxCe2O7-δ (M= Ca, Ba, Sr) catalyst for the low temperature oxidative coupling of methane: a combined DFT and experimental study, Chem. Eng. J. 458 (2023) 141379.

[58] Z. Hu, X. Liu, D. Meng, Y. Guo, Y. Guo, G. Lu, Effect of ceria crystal plane on the physicochemical and catalytic properties of Pd/ceria for CO and propane oxidation, ACS Catal. 6 (2016) 2265–2279.

[59] N. Wang, W. Qian, W. Chu, F. Wei, Crystal-plane effect of nanoscale CeO 2 on the catalytic performance of Ni/CeO 2 catalysts for methane dry reforming, Catal. Sci. Technol. 6 (2016) 3594–3605.

[60] B. Liu, C. Li, G. Zhang, X. Yao, S.S. Chuang, Z. Li, Oxygen vacancy promoting dimethyl carbonate synthesis from CO2 and methanol over Zr-doped CeO2 nanorods, ACS Catal. 8 (2018) 10446–10456.

[61] F. Wang, L. Xu, J. Yang, J. Zhang, L. Zhang, H. Li, Y. Zhao, H.X. Li, K. Wu, G.Q. Xu, Enhanced catalytic performance of Ir catalysts supported on ceria-based solid solutions for methane dry reforming reaction, Catal. Today 281 (2017) 295–303.

[62] Y.-L. Lee, A. Mnoyan, H.-S. Na, S.-Y. Ahn, K.-J. Kim, J.-O. Shim, K. Lee, H.-S. Roh, Comparison of the effects of the catalyst preparation method and CeO 2 morphology on the catalytic activity of Pt/CeO 2 catalysts for the water-gas shift reaction, Catal. Sci. Technol. 10 (2020) 6299–6308.

[63] S.O. Omarov, K.D. Martinson, A.N. Matveeva, M.I. Chebanenko, V. N. Nevedomskiy, V.I. Popkov, Renewable hydrogen production via glycerol steam reforming over Ni/CeO2 catalysts obtained by solution combustion method: the effect of Ni loading, Fuel Process. Technol. 236 (2022), 107429.

[64] A. Filtschew, K. Hofmann, C. Hess, Ceria and its defect structure: new insights from a combined spectroscopic approach, J. Phys. Chem. C. 120 (2016) 6694–6703.

[65] S. Loridant, Raman spectroscopy as a powerful tool to characterize ceria-based catalysts, Catal. Today 373 (2021) 98–111.

[66] Q. Li, Z. Yan, N. Wang, Z. Xu, G. Wang, G. Huang, 0D/2D CeO_2 quantum dot/NiO nanoplate supported an ultralow-content Pt catalyst for the efficient oxidation of formaldehyde at room temperature, Catal. Sci. Technol. 10 (2020) 4030–4041.

[67] S. Adak, R.S. Pal, T.S. Khan, M.K. Poddar, M.S. Ahmad, V.V. Prasad, M.A. Haider, R. Bal, Role of interfacial Cu-ions in polycrystalline $Cu-CeO_2$: in-situ raman, in-situ DRIFT and DFT studies for preferential oxidation of CO in presence of excess H2, ChemistrySelect 6 (2021) 13051–13059.

[68] J. Xu, R. Xi, Q. Xiao, X. Xu, L. Liu, S. Li, Y. Gong, Z. Zhang, X. Fang, X. Wang, Design of strontium stannate perovskites with different fine structures for the oxidative coupling of methane (OCM): Interpreting the functions of surface oxygen anions, basic sites and the structure–reactivity relationship, J. Catal. 408 (2022) 465–477.

[69] H. Chen, S. Chansai, S. Xu, S. Xu, Y. Mu, C. Hardacre, X. Fan, Dry reforming of methane on bimetallic Pt–Ni@ CeO_2 catalyst: a in situ DRIFTS-MS mechanistic study, Catal. Sci. Technol. 11 (2021) 5260–5272.

[70] L. Bobadilla, V. Garcilaso, M. Centeno, J. Odriozola, CO_2 reforming of methane over Ni-Ru supported catalysts: On the nature of active sites by operando DRIFTS study, J. CO_2 Util. 24 (2018) 509–515.

[71] M. Mao, Q. Zhang, Y. Yang, Y. Li, H. Huang, Z. Jiang, Q. Hu, X. Zhao, Solar-light-driven CO_2 reduction by methane on Pt nanocrystals partially embedded in mesoporous CeO_2 nanorods with high light-to-fuel efficiency, Green. Chem. 20 (2018) 2857–2869.

[72] F. Pompeo, N.N. Nichio, M.M. Souza, D.V. Cesar, O.A. Ferretti, M. Schmal, Study of Ni and Pt catalysts supported on α-Al2O3 and ZrO2 applied in methane reforming with CO_2, Appl. Catal. A: Gen. 316 (2007) 175–183.

[73] F.C. Meunier, Relevance of IR spectroscopy of adsorbed CO for the characterization of heterogeneous catalysts containing isolated atoms, J. Phys. Chem. C. 125 (2021) 21810–21823.

[74] S.M. Lee, Y.H. Lee, D.H. Moon, J.Y. Ahn, D.D. Nguyen, S.W. Chang, S.S. Kim, Reaction mechanism and catalytic impact of $Ni/CeO2–x$ catalyst for low-temperature CO_2 methanation, Ind. Eng. Chem. Res. 58 (2019) 8656–8662.

[75] L. Nie, D. Mei, H. Xiong, B. Peng, Z. Ren, X.I.P. Hernandez, A. DeLaRiva, M. Wang, M.H. Engelhard, L. Kovarik, Activation of surface lattice oxygen in single-atom Pt/$CeO2$ for low-temperature CO oxidation, Science 358 (2017) 1419–1423.

[76] F. Hu, R. Ye, C. Jin, D. Liu, X. Chen, C. Li, K.H. Lim, G. Song, T. Wang, G. Feng, Ni nanoparticles enclosed in highly mesoporous nanofibers with oxygen vacancies for efficient CO_2 methanation, Appl. Catal. B: Environ. 317 (2022), 121715.

[77] R.S. Pal, S. Rana, S. Sadhu, T.S. Khan, M.K. Poddar, R.K. Singha, S. Sarkar, R. Sharma, R. Bal, Highly active and selective Li/MgO catalysts for methane transformation to C 2 hydrocarbons: experimental and DFT study, Energy Adv. 2 (2023) 180–197.

[78] M. Shah, S. Das, A.K. Nayak, P. Mondal, A. Bordoloi, Smart designing of metal-support interface for imperishable dry reforming catalyst, Appl. Catal. A: Gen. 556 (2018) 137–154.

[79] J.-H. Kim, D.J. Suh, T.-J. Park, K.-L. Kim, Effect of metal particle size on coking during CO_2 reforming of CH4 over Ni–alumina aerogel catalysts, Appl. Catal. A: Gen. 197 (2000) 191–200.

[80] Z. Xie, B. Yan, J.H. Lee, Q. Wu, X. Li, B. Zhao, D. Su, L. Zhang, J.G. Chen, Effects of oxide supports on the CO_2 reforming of ethane over Pt-Ni bimetallic catalysts, Appl. Catal. B: Environ. 245 (2019) 376–388.

[81] V. Kroll, H. Swaan, C. Mirodatos, Methane reforming reaction with carbon dioxide over Ni/SiO2Catalyst: I. Deactivation studies, J. Catal. 161 (1996) 409–422.